A NUMERICAL MODEL BASED EXAMINATION OF CONDITIONS FOR IGNITIVE TURBIDITY CURRENTS

By

GOWTHAM KRISHNA

A THESIS PRESENTED TO THE GRADUATE SCHOOL
OF THE UNIVERSITY OF FLORIDA IN PARTIAL FULFILLMENT
OF THE REQUIREMENTS FOR THE DEGREE OF
MASTER OF SCIENCE

UNIVERSITY OF FLORIDA

2009

© 2009 Gowtham Krishna

To my Family

ACKNOWLEDEGMENT

First, I would like to thank my advisor Dr. Ashish J. Mehta, for all the guidance, support and knowledge that I received from him. Without him, this thesis would not have been completed. Special thanks go to other members of my committee including Dr. James F. Klausner and Dr. Robert G. Dean.

Thanks to my colleagues and office mates: Emre Ozdemir, who has been more than a friend to me and Sangdon So, for all the fun, humor and good times we have had. I would also like to thank all my colleagues from the department who have made my two years an enjoyable experience.

Lastly, but not the least I would like to thank my family for all the love and support they have given me.

TABLE OF CONTENTS

page

ACKNOWLEDEGMENT 4

LIST OF TABLES 7

LIST OF FIGURES 8

ABSTRACT 10

CHAPTER

1 INTRODUCTION 12

1.1 Study Motivation 12
1.2 Objective and Scope 14
1.3 Thesis Structure 15

2 TURBIDITY CURRENT:BACKGROUND 17

2.1 Definition of Turbidity Current 17
2.2 Early Investigations 17
2.3 The Structure of Gravity Current 19
2.4 Knapp-Bagnold Criterion for Suspension 23
2.5 Concluding Observation 28

3 TWO-PHASE EQUATIONS AND CLOSURES 31

3.1 Introduction 31
3.2 Two-Phase Flow Equations 32
3.3 Closure of Fluid Stresses 34
3.4 Closure of Sediment Stresses 38
3.4.1 Sediment Transport Equation 38
3.4.2 Collisional Theory of Granular Flow 40
3.4.3 Large Scale Sediment Stress 42
3.4.4 Closure at Low Concentrations 43
3.4.5 Region of Enduring Contact 44
3.5 Initial and Boundary Conditions 45
3.5.1 Initial Condition 45
3.5.2 Bottom Boundary Condition 46
3.5.3 Top Boundary Condition 47
3.5.4 Lateral Boundary Condition 49

4 NUMERICAL IMPLEMENTATION 50

4.1 Introduction 50
4.2 Mesh and Grid System 50
4.3 Numerical Discretization 51
4.3.1 Solution of Sediment Phase Equations 51
4.3.1.1 Predictor Step 52
4.3.1.2 Corrector Step 58
4.3.2 Fluid Phase Equations 59
4.4 Stability Analysis 61

5 RESULTS AND ANALYSIS 62

5.1 Preamble 62
5.2 Experimental Data and Model Output 64
5.3 Domain of Ignitive Behaviour 65

6 SUMMARY, CONCLUSIONS AND RECOMMENDATIONS 76

6.1 Summary 76
6.2 Conclusions 77
6.3 Recommendations for Further Work 79

APPENDIX

A Numerical Implementation Scheme 80

LIST OF REFERENCES 85

BIOGRAPHICAL SKETCH 88

LIST OF TABLES

Table		page
3-1	Summary of numerical coefficients adopted by the model	38
5-1	Model runs for grain size of 0.21mm	68
5-2	Model runs for grain size of 0.28mm	68
5-3	Model runs for grain size of 0.35mm	69
5-4	Flow state in experiment and model run	69
5-5	Flow states for 0.21mm particles	69
5-6	Flow states for 0.28mm particles	70
5-7	Flow states for 0.35mm particles	70

LIST OF FIGURES

Figure page

1-1 Diagrammatic definition of the continental shelf along with the continental slope and related geographic features. 16

2-1 Shadow pictures of the profiles of the head of the gravity current....29

2-2 Frontal region of a gravity current of saltwater advancing along the floor of a freshwater tank....29

2-3 Inviscid gravity current with mixing. The lower region (depth h_4) is unmixed saline solution, and the top region (h_2) is unmixed ambient fluid. Mixing takes place in the middle region of thickness h_3....29

2-4 Gravitational force components and velocities associated with the fluid and the solids. ...30

2-5 Schematic drawing of the experimental setup of Parker et al 30

5-1 Physical interpretation of mode simulations: (a) downstream gradient in pressure force leads to the development of a boundary layer velocity profile and associated profile in the suspended sediment concentration. Under non-ignitive conditions the concentration decreases due to sediment deposition; (b) conditions are conducive for ignition 71

5-2 Growth of boundary layer velocity and concentration profiles during a pre-test run with d = 0.21mm, u_* = 0.06 m/s and $\alpha = 0^o$ 71

5-3 Velocity and concentration profiles: Experimental data of Parker et al. (1987) and present model run. The main difference is in the grain size (0.03mm in experiment versus 0.20mm in the model). Both are at a distance of x=1.5m....72

5-4 Velocity and concentration profiles: Experimental data of Parker et al. (1987) and present model run. The main difference is in the grain size (0.03mm in experiment versus 0.20mm in the model). Both are at a distance of x=4.5m....72

5-5 Velocity and concentration profiles: Experimental data of Parker et al. (1987) and present model run. The main difference is in the grain size (0.03mm in experiment versus 0.20mm in the model). Both are at a distance of x=8.5m....73

5-6 Shields parameter against bed slope 73

5-7 Shields parameter against bed slope. Sediment flux per unit width (kg/m^3/s) contours for 0.21mm diameter particles 74

5-8 Shields parameter against bed slope. Sediment flux per unit width (kg/m^3/s) contours for 0.28mm diameter particles 74

5-9 Shields parameter against bed slope. Sediment flux per unit width (kg/m3/s) contours for 0.35mm diameter particles 75

5-10 Shields parameter against particle diameter. Threshold curves for incipient movement and auto-suspension curve. Model test run data 75

Abstract of Thesis Presented to the Graduate School
of the University of Florida in Partial Fulfillment of the
Requirements for the Degree of Master of Science

A NUMERICAL MODEL BASED EXAMINATION OF CONDITIONS FOR IGNITIVE TURBIDITY CURRENTS

By

Gowtham Krishna

December 2009

Chair: Ashish J. Mehta
Major: Coastal and Oceanographic Engineering

Turbidity currents form a major mechanism for the movement of sediment in the natural environment. Self-accelerating turbidity currents over continental slopes are of considerable scientific and engineering interest due to their role as agents for submarine sediment transportation from the shelf to the seabed. Such currents are called ignitive provided they eventually reach a catastrophic state as acceleration results in high sediment loads due to erosion of the sloping bed. In the present study ignition refers to the onset of self-acceleration and erosion characterized by positive values of the rate of change of current velocity and sediment flux down the slope. A numerical model, which treats the fluid and the particles as two separate phases, is applied to investigate the effects of particle size, initial flow friction velocity and mild bed slope on the ignitive condition. Laboratory experimental data of Parker et al. (1987) have been included as part of the analysis.

Ignition for the smallest of the three selected sizes (0.21mm) of medium sand typical of Florida beaches was found to depend on the initial conditions at the head of the slope as determined by the pressure gradient. Bed slope seemed to be of secondary importance. For the two sands with larger grain sizes (0.28mm and 0.35mm) the bed slope was found to play a more

important role when compared to the initial pressure gradient. For a given pressure gradient, increasing the slope increased the likelihood of self-acceleration. Thus, in general ignition cannot be defined merely in terms of non-trivial, positive values of the velocity gradient and the sediment flux gradient along the slope. Depending on particle size the initial pressure gradient can also play a role. For the selected initial conditions (grain size, pressure gradient and bed slope), out of the 54 combinations tested, all except three satisfied the Knapp-Bagnold criterion for auto-suspension irrespective of whether the turbidity current was ignitive or non-ignitive. In all 54 cases the current was found to erode the bed. Further use of the model will require accommodation of wider ranges of sediment size and bed density, and a thorough verification against experimental data.

CHAPTER 1
INTRODUCTION

1.1 Study Motivation

A flow resulting from density difference due to spatial variability in the suspended sediment concentration is known as a turbidity current. In nature turbidity currents are witnessed in a variety of environments. The major difference between density currents due to dissolved substances such as salt or due to the effect of temperature on density on one hand, and turbidity currents on the other is the potential ability of the turbidity current to deposit sediment on the bed. Unlike the movement of bedload or suspended load of sediment due to water flow, a turbid current can also move through otherwise still water as a diffusion-induced front.

Turbidity currents form a major mechanism for the transport of continental shelf sediment into deeper waters. They commonly occur on the shelf due to inflow of turbid waters from riverine sources (Fig. 1.1). Closer to the river mouth, they may persist as underflows over the foreset slope of the clinoform delta. By way of transport of sediment from the shelf to the continental slope, and then into the deeper oceanic waters, turbidity currents are believed to be responsible for breaks in submarine pipelines and telephone cables. The current can erode a submarine channel analogous to a river, and sediment thus transported will contribute to the development of the seabed.

Self-accelerating turbidity currents is a topic of considerable scientific and engineering interest, because such currents can be responsible for significant transport of sediment from terrestrial sources to the seabed. Self-acceleration can occur if the flow velocity and the suspended sediment concentration increase simultaneously as bed sediment erodes due to the impelling down-slope gravity force and associated turbulence.

Self-acceleration in the present study is defined as the condition when the turbid current generates sufficient turbulence to hold the particles in suspension. It causes the bed to erode, particles are picked up and the suspension becomes denser. As a result, acceleration increases, more sediment is picked up and the suspension becomes even denser. "Ignition" in this case can be considered to refer to the onset of self-acceleration without reference to its subsequent fate.

Self-acceleration necessarily included a condition in which erosion occurs and its rate is greater than that rate of deposition. Knapp (1938) referred to the process of ignition as "auto-suspension", a term he is believed to have coined. However, the subsequently derived criterion for auto-suspension by Bagnold (1962) is based on the condition of equilibrium between eroding bed sediment and depositing suspended (as opposed to bedload) sediment. Thus the criterion for auto-suspension is a necessary but not a sufficient condition for self-acceleration of sediment suspended in a current (Parker, 1982). A restraining influence on an ignitive turbidity current is that the self-sustaining property of the current ceases to exist either due to non-availability of sediment or due to damping of turbulence caused by the excess suspended sediment. When the flow becomes saturated with sediment turbulence collapse can occur (Winterwerp, 1999). The present study is concerned only with conditions that lead to ignition. Turbulence collapse is a catastrophic condition that is not considered in the present analysis.

Because of the submersed locations and scales of natural turbidity currents in the sea, it has been difficult to collect data on self-acceleration in the field. As a result, although self-sustaining currents have been postulated to occur on continental slopes, especially close to the seafloor, little is known about their incipient, ignitive dynamics, which is complicated by strong interactions between the sediment particles and water flow. Therefore, to understand the mechanism of self-acceleration in detail, mathematical models have been developed to simulate

the onset of turbidity currents in the natural environment. Although such models do not fulfill the need for field data, they are useful for developing broad criteria meant to identify conditions under which self-acceleration or ignition occurs. However, most modeling has been based on the use of a single fluid assumed to represent a suspension of sedimentary particles. The modeling approach selected for the present study considers the fluid (water) and sediment as two separate phases.

1.2 Objective and Scope

In a vertical, one-dimensional (1DV) model, two-phase flow equations for the fluid and the sediment are used to examine the effects of important factors resulting in self-acceleration of turbidity currents. The analysis has been carried out within the framework of the well-known Knapp-Bagnold criterion for auto-suspension of sediment particles in turbulent flows.

The mathematical model has been stated with the basic equations of continuity and momentum for the two phases, as well as the closure schemes and approximations considered. Since the 1DV model is restricted to the coordinate perpendicular to the bed, a vertical column is considered in which essential fluid and sediment properties and dynamic behaviors are described. Initially, a pressure gradient is used as a forcing condition to achieve a fully (or nearly fully) developed boundary layer flow without taking the bed slope into account, as the gravity force acts in the direction perpendicular to the bed. To simulate the subsequent flow conditions over a slope (with a prescribed bed sediment concentration), which is assumed to be mild, the pressure force is switched off and the effects of the gravity components in the pseudo-streamwise and vertical directions are invoked. Values of the velocity and sediment concentration are noted at different elevations and times. Based on the depth-mean current velocity, the vertical profiles of velocity and concentration can be translated by calculating the approximate distance traveled during each (selected) elapsed time. The sediment flux is then calculated at selected distances

from the start of the slope corresponding to the times of velocity and concentration "sampling" in the model.

The model is run (numerically) for a range of initial conditions with respect to particle size, the pressure gradient and bed slope in order to identify the domain within which the system is ignitive, i.e. for which self-acceleration occurs.

1.3 Thesis Structure

This thesis is organized into five chapters. Chapter 2 gives a brief introduction to turbidity currents. The main factors affecting gravity currents in general and the place of turbidity currents within the classification of gravity currents are mentioned. Also, a review of studies relevant to the analysis of the model output (in Chapter 5) is presented.

Chapter 3 mentions two numerical approaches employed in computing multiphase flows, including the Euler-Euler approach and the Euler-Euler approach (used in the present case). Then the governing equations of two-phase flow and their respective closure schemes are described.

Chapter 4 presents the numerical method applied to solve the governing equations along with the initial and boundary conditions using the finite difference approximation.

In Chapter 5 the results from model applications are presented and discussed. Selective data sets from studies mentioned in Chapter 2 have been used to corroborate the findings related to the parametric domain of ignitive turbidity currents within the framework of the Knapp-Bagnold criterion (also described in Chapter 3).

Conclusions based on this analysis and suggestions for further work are given in Chapter 6. In Appendix A, the numerical implementation of the code is given as a flow chart.

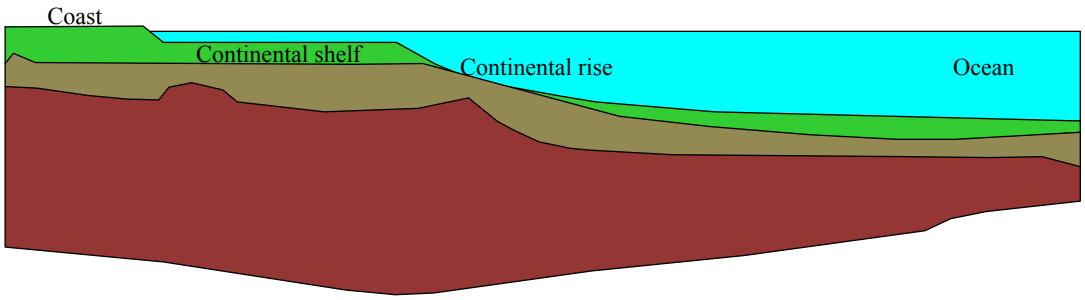

Figure 1.1 Diagrammatic definition of the continental shelf along with the continental slope and related geographic features.

CHAPTER 2
TURBIDITY CURRENTS: BACKGROUND

2.1 Definition of Turbidity Current

Information related to the turbidity current in this and the next two sections (2.2 and 2.3) is meant to provide the reader a general background on turbidity currents. The description of auto-suspension in Section 2.4 is directly related to the analysis presented in Chapter 5.

Turbidity currents are flows of sediment-laden fluid down a slope or along a horizontal surface through water or another fluid. Under certain circumstances the current may not be merely self-sustaining but also self-reinforcing, using the bed sediment as "fuel" to reach a catastrophic condition.

Turbidity currents can be characterized by a distinctive raised front or head followed by a quasi-uniform flow region. Experiments by Schmidt (1911) showed (Fig. 2.1) the way by which density difference corresponding to a temperature difference influence the shape of the head. The temperature is raised form a few degrees in (a) to 9°C in (f) corresponding to a density difference of 1%. The raised nose and the instabilities at the top surface can be seen from (a) to (f). Figure 2.2 shows the front of a gravity current of salt water advancing in freshwater. The head can be a zone of intense fluid mixing and interfacial wave breaking. Billows on the upper surface of the head may grow and break up into a three-dimensional pattern leaving behind a mixed layer. Another distinct feature of the turbidity current is the exchange of the granular particles between the current and the bed.

2.2 Early Investigations

An earthquake at the Grand Banks of the south coast of Newfoundland (Canada) triggered a turbidity current at estimated speeds of 60-100 km/h (Fine et al., 2005). The earthquake created a large submarine landslide that led to the breakage of 12 submarine telegraph cables and

resulted in a tsunami. Heezen and Ewing (1952) and Heezen et al. (1954) provided evidence that the break in the telegraph cables was caused by a self-accelerating turbidity current.

As an explanation for the origin of submarine canyons, Daly (1936) proposed that they were possibly cut by turbidity currents. Kuenen (1937) carried out supportive experiments in the laboratory to test Daly's hypothesis. Theoretical and experimental investigations by Knapp (1938) are also among the early works of turbidity and conservative gravity currents. Later, Middleton (1966a, 1966c) carried out a series of laboratory experiments to study the frontal head. He also described laws concerning the uniform flow of density currents and the deposition of sediment by turbidity currents. Plapp and Mitchell (1960) provided one of the first models for turbidity currents. Most of the early models considered turbidity currents to be analogous to conservative gravity flows. Chu et al. (1979) presented an analytical model specifically for turbidity current dynamics. They derived the governing equations of motions for the continuity of mass and momentum for the solid and the liquid phases and a diffusion equation for the rate of change of the suspended sediment within the control volume. Parker (1982) examined turbidity currents applying a "slab" model and investigated the state of "ignition" at which the flow entrains sediment and accelerates the current to a "catastrophic" state. McTigue (1981) used two-phase flow equations to study sediment transport due to turbidity currents, while Greimann et al. (1999) applied two-phase flow equations to turbid channel flows.

Lin and Mehta (1997) studied the depositional turbidity currents and the accompanying sediment transport that takes place in long and shallow closed-end basins. The experiment simulated a lock exchange setup where the ambient fluid consisted of fresh water and in different test runs sediment laden dense fluid consisted either of kaolinite, flyash or mud. They show that

along the length of the basin the settling velocity decays exponentially with distance and the rate of accumulation of sediments is highest near the entrance and decreases with distance.

2.3 Structure of Gravity Currents

In gravity currents moving on a horizontal surface the head remains in a quasi-steady state unlike in flow over a slope where the head increases in size with increasing angle of bed inclination. The front advancing over a rigid bed will have its foremost point elevated as a result of the no-slip condition acting at the lower boundary. This feature is the nose. The shape of the head/nose does not conform to any unique outline as it changes with the depth of the ambient fluid. Other factors that affect the head shape are the physical properties of the two fluids and bed roughness. Flow turbulence and current direction, whether opposing or flowing into the ambient flow, also play a role in determining head shape.

Turbulence-induced mixing is a important feature of the head of gravity current. There are two main kinds of instabilities which cause turbulence mixing:

- Billows: Due to the well-known Kelvin-Helmholtz instability, billows are formed on the upper surface of the head and roll up in the region of velocity shear above the front.
- Lobes and clefts: Due to the elevated frontal nose, as the current advances some of the lighter fluid in its path is disturbed resulting in instability.

Most attempts at understanding the head of the gravity current have been from the standpoint of a conservative current. However, a comparison of the heads of turbidity current with saline gravity current was done by Middleton (1966a). The basic characteristics influencing the head on a horizontal bed have been discussed in a general sense and these have also been applied to the heads of a gravity current including a turbidity current on slopes.

The inviscid fluid theory has been applied to study features of steady gravity currents such as wave breaking. The propagation of an immiscible gravity current over a frictionless surface was first proposed by Von Karman (1940). Even in the absence of frictional forces, instabilities leading to the formation of billows can be shown to occur. In the absence of friction the tip of the gravity current would touch the boundary indicating the absence of a nose. Von Karman considered that the interface would become parallel to the surface at a large distance behind the head and there the velocity would be constant.

Von Karman applied the Bernoulli equation between the tip of the current (which in this case touches the ground) where the stagnation point exists and along the interface far upstream and obtained the relation

$$U_f = \sqrt{2g'H_f} \tag{2.1}$$

Where, H_f is the head height, g' is the reduced gravity and U_f is the propagation velocity.

Benjamin (1968) investigated the front of the frictionless gravity current in terms of a cavity current, i.e. an empty cavity advancing in a liquid displacing the fluid beneath.

He calculated U_f from the continuity equation and H_f from the Bernoulli equation applied at the interface. For frictionless flow the pressure force and the momentum flux per unit mass are conserved. The result is that if the current height h is assumed equal to H_f, it will also be equal to one-half the total water depth H of the ambient fluid, i.e. $h=H/2$. This implies that the gravity current can progress steadily if it fills one-half the height of the ambient fluid. If $h>H/2$, then external supply of energy would be necessary to sustain the flow and this is not possible; whereas if $h<H/2$, energy loss at the front results from wave breaking.

Britter and Simpson (1978) carried out a semi-empirical analysis in which the surface is assumed to be smooth but mixing is allowed to take place between the gravity current and the ambient fluid, as for example in the case of large-scale gravity currents of saltwater displacing freshwater at tidal or river locks, where frontal mixing occurs.

The apparatus consisted of a flexible conveyor belt which could move at the speed of the current effectively giving rise to the slip condition, thereby simulating a frictionless surface. The experiment represented a gravity current of a dense fluid (saline solution) miscible with the ambient fluid (freshwater) and moving along the surface effectively in the absence of friction. The difference when compared to Von Karman (1940) was that the fluid in Von Karman's analysis was immiscible unlike the present case. In the Britter and Simpson investigation the head was found to be divided into three regions. The bottom region represented the flow of unmixed dense fluid into the gravity current. The topmost region consisted of only the unmixed, less dense the ambient fluid. Between these two regions was the layer in which mixing took place. This region had non-uniform velocity and salinity profiles.

The Britter and Simpson apparatus also made it possible to investigate the properties of billows at the front. It was found that they had the properties of Kevin-Helmholtz instabilities. Such instabilities could occur for a certain ranges of values of the relative velocity U between the two fluids, distance traveled and the density difference in terms of reduced gravity. Based on the Richardson number $Ri = g'h/U$ it was observed that the instabilities occurred for $Ri<1/4$.

In a flow with no-slip condition (due to the friction) at the lower boundary, the less dense fluid accumulated underneath the nose ascends as the front moves forward, and the associated instabilities occur as unsteady lobes and clefts. Billows still remain as the main feature within which the ambient fluid is mixed with the gravity current (Britter and Simpson, 1979).

Experiments (Simpson, 1972) have shown that it is feasible to suppress the unstable lobes and clefts by overrunning the less dense fluid with a layer of denser fluid. Simpson and Britter (1980) conducted laboratory experiments describing the nose height in relation to the head of the current as a function of the Reynolds number, $\mathrm{Re} = U_1(h_3 + h_4)/\nu$, where U_1 is the speed of the opposing flow, $h_3 + h_4$ is the height from the floor to the top of the mixed layer and v is the kinematic viscosity of water (Fig 2.3).

As mentioned, the turbidity current is a special case of a large class of gravity flows. The following classification of gravity flows (Altinakar 1988) is based on the density difference of the entering fluid and the state of stratification of the ambient fluid.

1. If the entering fluid is denser than the ambient fluid then the current plunges to the bottom and is known as an undercurrent or a bottom gravity current.
2. If the entering fluid is lighter than the ambient fluid, the current will occur on top of the ambient fluid, also called an overflow.
3. In case the ambient fluid is a stably stratified, different scenarios are possible depending on the density of the entering fluid relative to the ambient fluid. For example, if the density of the entering fluid has an intermediate value between the lowest and the highest densities of the stratified ambient fluid, an intermediate or intrusion type of current is formed at the appropriate density level.

When the gravity current is due to temperature or dissolved matter, the buoyancy flux, i.e. the flux of excess body force through a section of a current, is defined as $B = (\Delta\rho / \rho_a)gq$, where $\Delta\rho$ is the density difference between the fluid comprising the current and the ambient fluid, ρ_a is the density of the ambient fluid, g is the acceleration due to gravity and q is the discharge per unit width. Note that the reduced gravity $g' = g\Delta\rho / \rho_a$. The buoyancy flux is conserved

throughout the current. In contrast, in a turbid current this may not be the case as the current may erode the bed sediment or permit deposition of the suspended particles.

2.4 Knapp-Bagnold Criterion for Suspension

Knapp (1938) was one of the earliest investigators to explore the basic criterion for the transport of granular materials in suspension. He hypothesized the concept of auto-suspension stating that sediment particles in a flowing stream add or subtract energy through two independent processes. If the amount of energy added per unit time is less than the amount subtracted per unit time then the net result would be that the particles would become a burden on the stream, further implying that the there must a definite limit to the number of such particles that can be kept in suspension. On the other hand, if the amount of energy added is greater than the amount subtracted, then the energy of the stream is increased by the presence of the particle. This would indicate that there would be no limit to the number of particles kept in suspension and transported by (a unit volume of) the fluid. The resulting flow is an auto-suspension. Bagnold (1962) developed Knapp's arguments and suggested a criterion by examining suspended sediment transport in a laboratory setup.

The physical condition considered was a gently sloping bed which enabled a turbid suspension as well as sedimentation of sand and silt to occur, with turbulence as the cause of resuspension (Fig 2.4).

The mass m of the suspended sediment steadily falls but the center of gravity of the suspended sediment stays above the bed, because turbulence acts in the opposing direction in keeping the sediment suspended .The force due to turbulence should be acting against the immersed weight of the mass with fall velocity w_s .The power required to do so given by

$$\frac{\rho_s - \rho_f}{\rho_s} g m w_s \tag{2.2}$$

Where ρ_s is the sediment density and ρ_f the fluid density.

The power expended by the fluid is replenished by the tangential pull acting on the suspension by the down-slope gravity component. This is given by

$$\frac{\rho_s - \rho_f}{\rho_s} g m \overline{U} \sin\beta \tag{2.3}$$

Where $\overline{U}$ is the speed of the solids traveling downstream, and β is the angle of bed inclination with the horizontal. Therefore the net power expended by the fluid in keeping the sediment suspended is given by

$$\frac{\rho_s - \rho_f}{\rho_s} g m \overline{U} (w_s / \overline{U} - \sin\beta) \tag{2.4}$$

When the sediment size is decreased this term becomes zero independent of the magnitude of the mass. Therefore,

$$w_s = \overline{U} \sin\beta \tag{2.5}$$

As the bed slope increases the power provided by the tangential gravity component is sufficient not only to keep the sediment suspended but also to contribute to the power needed against fluid drag at the boundary. The total power due to available sediment is given by

$$(\rho_s - \rho_f) g \overline{C} h \overline{U} \sin\beta \tag{2.6}$$

Where, $\overline{C}$ is the mean sediment concentration and h is the flow height. To maintain the suspension the power expended is

$$(\rho_s - \rho_f) g \overline{C} h v \tag{2.7}$$

Therefore, the excess power needed for flow against drag is given as

$$(\rho_s - \rho_f) g \overline{C} h (\overline{U} \sin\beta - w_s) \tag{2.8}$$

The power needed to maintain mean velocity $\overline{u}$ is $\tau_0 \overline{u}$, where τ_0 is the bed shear stress. From Francis (1957) $\tau_0 \overline{u}$ is given as

$$\tau_o \overline{u} = \frac{\rho \overline{u}^3}{33} \log_{10}^{-2} \frac{13.2h}{k} \tag{2.9}$$

From this development Bagnold concluded that the criterion for a self-sustained turbidity current is given by,

$$(\rho_s - \rho_f) g \overline{C} h \overline{U} \left(\sin\beta - \frac{w_s}{\overline{u}} \right) \geq \frac{\rho \overline{u}^3}{33} \log_{10}^{-2} \frac{13.2h}{k} \tag{2.10}$$

Middleton (1966a) stated that this theory contains a number of doubtful and overly simplified assumptions. He maintained that Bagnold ignored the resistance at the upper interface, sediment sorting and concentration effects. The form of Bagnold's criterion from equation (2.5) suggests that for larger ratios of settling velocity to the horizontal velocity, auto-suspension is possible for larger slopes. Middleton contended that an increase in the slope would increase the Froude number due to which mixing and resistance would rapidly increase at the upper interface. This in turn would indicate that the optimum conditions for obtaining auto-suspension may be at low slopes. Middleton also questioned the inequality $Us / w_s \geq 1$, where U is the mean fluid velocity, which should be an equality instead. Middleton did not provide an alternative auto-suspension criterion; however, he stated that the ideal conditions in which auto-suspension would be favorable would be a combination of the presence of fine grained sediment, low sediment density and a relatively large physical model scale.

Pantin (1979) argued that the energy budget considered by Bagnold was incomplete and incorrect. In Bagnold's hypothesis the total available power from equation (2.6) may be denoted by the symbol *w*. The energy needed to keep the sediment suspended is given by equation (2.7). Let this energy be denoted by the symbol w_n and let the work expended against bottom friction, $\tau_0 \bar{u}$, be denoted as w_t . The essential power condition given by Bagnold in his auto-suspension criterion can be summarized as

$$w \geq w_n + w_t \tag{2.11}$$

However, Pantin contended that this condition is not valid because the power expended in supporting suspended sediment would be independent of the power expended against bottom friction. He noted that the power needed to support sediment in suspension would be derived from turbulence within the fluid and the necessary power required to support turbulence itself derived from the work expended against bottom friction. Therefore w_n is part of w_t and the remainder of w_t is dissipated as micro-turbulence and eventually heat, which has little influence in keeping the sediment suspended. Therefore Pantin redefined the power involved by the following relationships

$$w \geq w_t \quad \text{and} \quad e_x w_t \geq w_n \tag{2.12}$$

Where e_x is an efficiency factor. A large efficiency e_x would promote auto-suspension.

Parker (1982) studied the conditions under which ignition of "catastrophically erosive turbidity currents" is possible. He mentioned that the Bagnold criterion $Us / w_s \geq 1$ is a necessary but not a sufficient condition for ignition. He presented a three-equation model explaining the process involved in ignition. Parker et al. (1986) proposed a more refined four-equation model

by adding the equation of mean turbulence energy to the conservation equations for fluid mass and sediment as well as conservation of momentum of the mixture, and solved the equations numerically to investigate the possibility of self-accelerating turbidity current. Parker et al. (1986) observed that the earlier three-equation model does not account for the turbulent energy balance and the solutions thus obtained are physically not possible.

Following the development of the four-equation model, Parker et al. (1987) conducted laboratory tests to determine the behavior of turbidity currents. The experiments consisted of currents laden with non-cohesive sediment (silica flour) on a sloping bed in a channel which was covered with the same sediment (Fig 2.5). The velocity and concentration profiles were measured at three locations along the channel. The results obtained were used to calculate "top-hat" functions used in the mathematical model of Parker et al (1986). Let the local mean velocity, volumetric sediment concentration and the mean kinetic energy per unit mass be denoted by u, c and k, the layer thickness h and the corresponding layer averages U,C and K. Then the following similarity laws were assumed

$$\frac{u(x,z)}{U(x)} = \zeta_u(\eta); \quad \frac{c(x,z)}{C(x)} = \zeta_c(\eta); \quad \frac{k(x,z)}{K(x)} = \zeta_k(\eta) \tag{2.13}$$

Where

$$\eta = \frac{z}{h} \tag{2.14}$$

The top-hat functions are defined such that

$$\zeta_u(\eta) = \zeta_c(\eta) = \zeta_k(\eta) = \begin{cases} 1 \; if \;\; 0 < \eta < 1 \\ 0 \; if \;\; \eta > 1 \end{cases} \tag{2.15}$$

The current was considered to be ignitive when the rate of change of current over distance was positive and the the rate of change of sediment flux over distance was also positive. Based on this definition, two of the 23 runs were shown to generate an ignitive turbidity current. Unfortunately, the ensuing catastrophic condition could not be recorded as the experimental facility was too short.

Eidsvik and Brors (1989) studied self-acceleration of turbidity currents using an algebraic closure model and also the κ-ε model; they presented results using the latter closure model only. They assumed the sediment volume concentration to be very small and predicted the general structure of an ignitive turbidity current by showing an increase in the velocity, concentration and the turbulent kinetic energy profiles over an extended period of time. They simulated conditions applicable to fine grain sediment and small slopes. They predicted that ignition can occur at very small angles.

2.5 Concluding Observation

Most mathematical models have treated the turbidity current as a single-phase conservative current, which makes the analysis approximate and therefore somewhat qualitative. Therefore an attempt has been made in the present study to look into the phenomenon of ignition through the use of a two-phase model in which the role of sediment is included explicitly. Also, the inclusion of the turbulent suspension flux term and particle stresses due to inter-particle interactions does not require the imposition of a sediment pick-up function, or equations for bedload and suspended load transport.

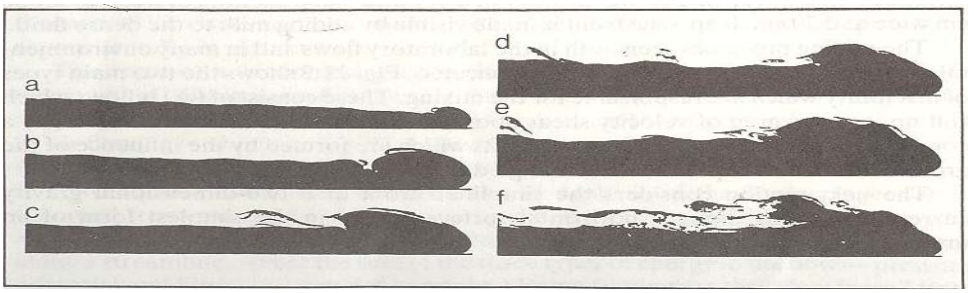

Figure 2.1 Shadow pictures of the profiles of the head of the gravity current (Source: Simpson, 1987).

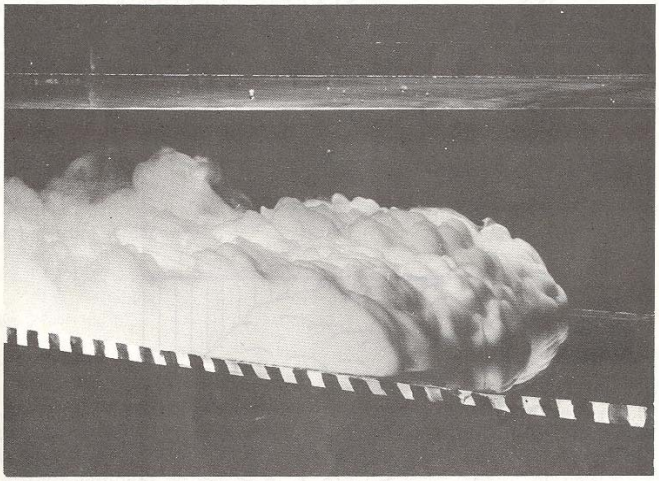

Figure 2.2 Frontal region of a gravity current of saltwater advancing along the floor of a freshwater tank (Source: Simpson, 1987).

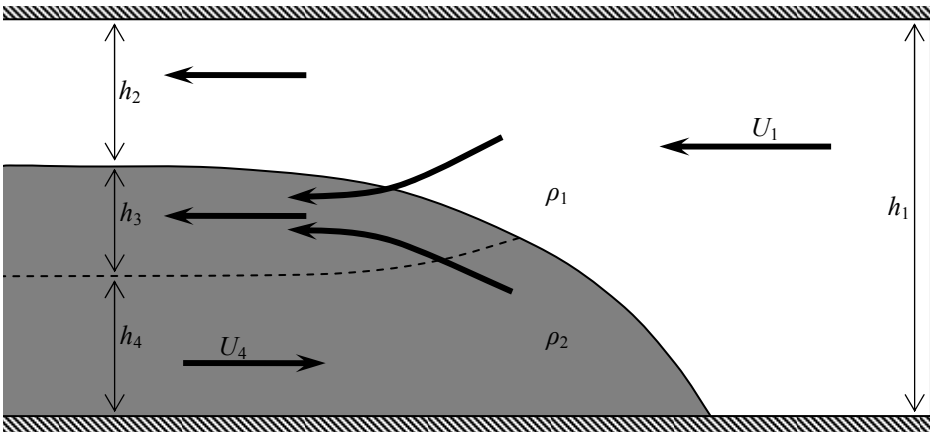

Figure 2.3 Inviscid gravity current with mixing. The lower region (depth h_4) is unmixed saline solution, and the top region (h_2) is unmixed ambient fluid. Mixing takes place in the middle region of thickness h_3 (Adapted from Simpson, 1987).

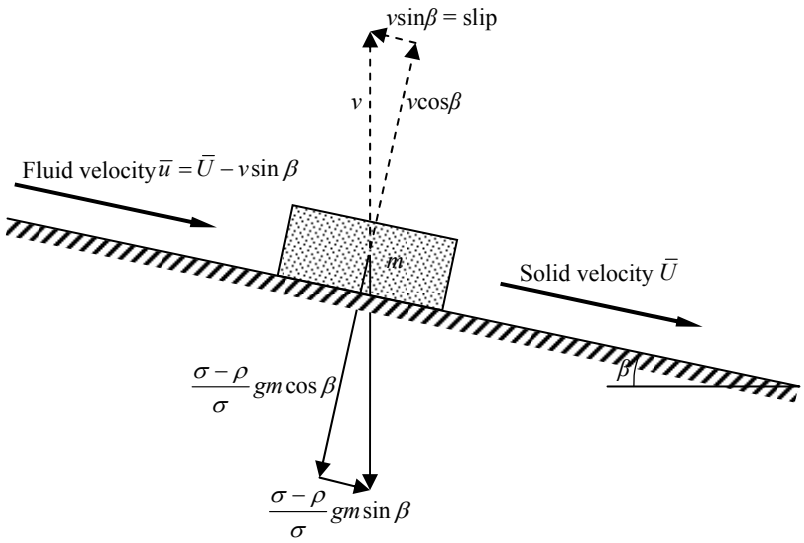

Figure 2.4 Gravitational force components and velocities associated with the fluid and the solids (Source: Bagnold, 1962).

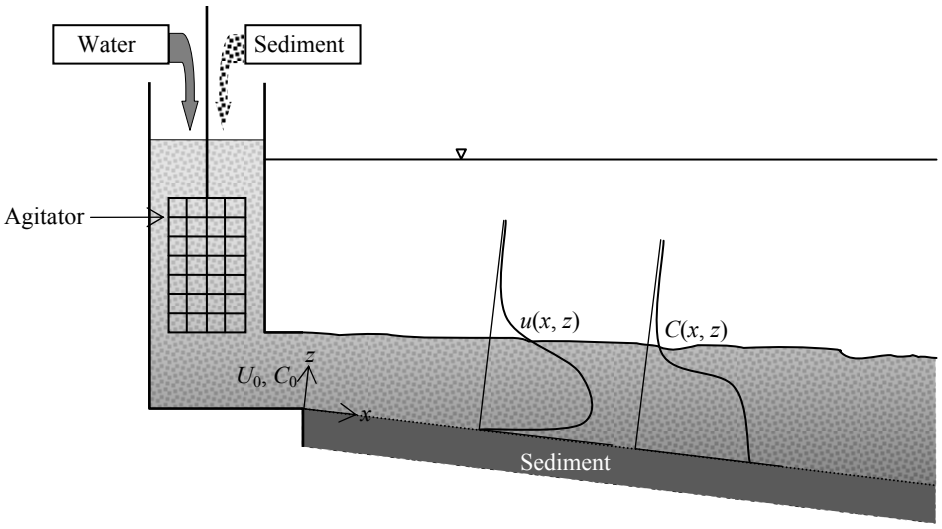

Figure 2.5 Schematic drawing of the experimental setup of Parker et al. (1987).

CHAPTER 3
TWO-PHASE EQUATIONS AND CLOSURES

3.1 Introduction

A large number of flow regimes in nature can be interpreted as mixtures of two phases. Different sizes of the same material can be dealt with as separate phases. In multiphase flow a phase can be identified from its interaction with the flow fluid. For example gas-solid flows (particle laden flows), gas-liquid flows (bubbles in continuous fluid), liquid-liquid flows (immiscible fluids separated by a discernible inter-phase), liquid-solid flows (slurry flow) and three-phase flows (a combination of the above) can be said to be the major classification regimes of a multiphase flow.

The numerical approach of computing multiphase flows can be broadly classified into two categories: Euler-Lagrange and Euler-Euler.

Euler-Lagrange Approach: The fluid is treated as a continuum and the time averaged Navier Stokes equations are used to solve them. Dispersed particles are treated by tracking a large number of them through the flow field. A basic assumption made in the present study is that the second phase occupies a low volume-concentration and has no direct impact either on the generation or dissipation of turbulence.

Euler-Euler Approach: In this approach both the phases are treated as inter-penetrating continua. The derived conservation equations for the phases are consistent with each other and have similar structures. These equations are coupled through pressure or the inter-phase exchange coefficient. This approach is computationally more expensive as it evaluates more equations, but is also more accurate. This approach was therefore used.

Sediment transport in water is a two-phase phenomenon. For the most exhaustive treatment of sediment transport one can assume fluid flow to be governed by the Navier-Stokes equations and the action of every sediment particle can be considered through its corresponding equation of motion. However, as this is not pragmatic, the sediment particles will be considered as part of a continuum. Accordingly, the equations of motion for the two phases have the same form. Ensemble averages of the mass and momentum equations are considered. As part of this averaging the definition of sediment concentration *c* is introduced.

3.2 Two-Phase Flow Equations

Ensemble averaging is carried out over a size of the order of the grain diameter, but the sediment concentration fluctuates on a scale much larger than the grain diameter, hence another averaging process is required (Hsu et al., 2003). This process, i.e. Favre averaging, is carried out on the already averaged two-phase flow equations. The Favre averaged fluid-phase continuity equation is

$$\frac{\partial}{\partial t}\rho^f(1-\overline{c})+\frac{\partial}{\partial z}\rho^f(1-\overline{c})\overline{w}^f=0 \tag{3.1}$$

and the sediment-phase continuity equation is

$$\frac{\partial}{\partial t}\rho^s\overline{c}+\frac{\partial}{\partial z}\rho^s\overline{cw}^s=0 \tag{3.2}$$

Where ρ^f the mass density of water. Sediment particles are assumed to have the same diameter *d* with mass density ρ^s, *z* is the normal axis component to the bottom, and $\overline{w}^f$, $\overline{w}^s$ are the *z*-direction averaged fluid and particle velocities, respectively.

Let us consider the fluid-phase momentum equations in the *x*-direction:

$$\frac{\partial}{\partial t}\rho^f(1-\overline{c})\overline{u}^f = -\frac{\partial}{\partial z}\rho^f(1-\overline{c})\overline{u}^f\overline{w}^f - (1-\overline{c})\frac{\partial \overline{P}^f}{\partial x} + \frac{\partial \tau^f{}_{xz}}{\partial z} - \rho^f(1-\overline{c})Sg - \beta\overline{c}\left(\overline{u}^f - \overline{u}^s\right) \tag{3.3}$$

and in the z-direction:

$$\frac{\partial}{\partial t}\rho^f(1-\overline{c})\overline{w}^f = -\frac{\partial}{\partial z}\rho^f(1-\overline{c})\overline{w}^f\overline{w}^f - (1-\overline{c})\frac{\partial \overline{P}^f}{\partial z} + \frac{\partial \tau^f{}_{zz}}{\partial z} + \rho^f(1-\overline{c})g - \beta\overline{c}\left(\overline{w}^f - \overline{w}^s\right) + \beta\upsilon_{ft}\frac{\partial \overline{c}}{\partial z} \tag{3.4}$$

Where $\overline{u}^f$ and $\overline{u}^s$ are the averaged fluid and sediment horizontal velocities, respectively, S= slope, $\overline{P}^f$ is the ensemble averaged fluid pressure, and τ^f_{xz}, τ^f_{zz} are the average fluid-phase stresses including, in both cases, the viscous stress and the fluid phase Reynolds stress. The remaining terms in the above equations, apart from the first term on the left hand side, which is the unsteady term, and the first term on the right hand side, which is the convective term, the remaining terms indicate Favre averaged drag forces due to fluid-sediment interaction and the relative mean velocity between the two phases, and β is the drag coefficient given by

$$\beta = \frac{\rho^f U_r}{d}\left(\frac{18.0}{\mathrm{Re}_p} + 0.3\right)\frac{1}{(1-\overline{c})^n} \tag{3.5}$$

Where the concentration dependence is taken from the work of Richardson and Zaki (1954) on hindered settling and U_r is the relative velocity between the fluid and sediment phase velocities given as,

$$U_r = \sqrt{\left(\overline{u}^f - \overline{u}^s\right)^2 + \left(\overline{w}^f - \overline{w}^s\right)^2} \tag{3.6}$$

If the dynamic viscosity is denoted μ_f, the particle Reynolds number is given by

$$\mathrm{Re}_p = \frac{\rho^f U_r d}{\mu_f} \tag{3.7}$$

The exponent n in (3.5), which depends on the particle Reynolds number, is given by

$$n = \frac{4.45}{\mathrm{Re}_p} \tag{3.8}$$

The corresponding sediment-phase momentum equations are given as below, in the x-direction as

$$\frac{\partial}{\partial t}\rho^s \overline{c}\,\overline{u}^s = -\frac{\partial}{\partial z}\rho^s \overline{c}\,\overline{u}^s \overline{w}^s - \overline{c}\frac{\partial \overline{P}^f}{\partial x} + \frac{\partial \tau^s{}_{xz}}{\partial z} - \rho^s \overline{c} S g + \beta \overline{c}\left(\overline{u}^f - \overline{u}^s\right) \tag{3.9}$$

and in the z-direction as,

$$\begin{aligned}\frac{\partial}{\partial t}\rho^s \overline{cw}^s = &-\frac{\partial}{\partial z}\rho^s \overline{cw}^s \overline{w}^s - \overline{c}\frac{\partial \overline{P}^f}{\partial x} \\ &+ \frac{\partial \tau^s{}_{zz}}{\partial z} + \rho^s \overline{c} g + \beta \overline{c}\left(\overline{u}^f - \overline{u}^s\right) - \beta \upsilon_{ft}\frac{\partial \overline{c}}{\partial z}\end{aligned} \tag{3.10}$$

The last term in equations (3.4) and (3.10) is the correlation between concentration fluctuations and the fluid velocity fluctuations. It represents the sediment flux caused by large-scale fluid turbulence.

The parameters τ^s_{xz} and τ^s_{zz} are the average stresses in the sediment phase. Each stress includes contributions from inter-particle collisions and sediment-fluid interaction and the Reynolds stress due to the velocity fluctuations of the particles.

3.3 Closure of Fluid Stresses

The total stresses in the fluid phase can be written as

$$\tau^f_{xz} = \tau^{f0}_{xz} + R^f_{xz}; \qquad \tau^f_{zz} = \tau^{f0}_{zz} + R^f_{zz} \tag{3.11}$$

Where τ_{xz}^{f0} and τ_{zz}^{f0} are the average small-scale stresses consisting of the viscous stress and the small-scale Reynolds stress due to turbulence between the particles or due to particle fluctuations. The Favre averaging process results in large-scale Reynolds stresses R_{xz}^{f} and R_{zz}^{f} due to turbulent fluctuations in which concentration fluctuation is taken in to account. These Reynolds stresses are defined as correlations between the concentration and velocity fluctuations representing the transfer of momentum and are given as

$$R_{xz}^{f} = -\rho^{f}(1-c)\Delta u^{f}\Delta w^{f}; \qquad R_{zz}^{f} - = -\rho^{f}(1-c)\Delta w^{f}\Delta w^{f} \tag{3.12}$$

Turbulent eddy viscosity parameterization is used to solve for the large-scale fluid Reynolds stresses. Applying the current closure schemes the stresses are given as

$$\tau_{xz}^{f} = \rho^{f}\left(\upsilon_{ft} + \upsilon_{f}\right)\frac{\partial \overline{u}^{f}}{\partial z} \tag{3.13}$$

and

$$\tau_{zz}^{f} = -\frac{2}{3}\rho^{f}(1-\overline{c})k_{f} + \frac{4}{3}\rho^{f}\left(\upsilon_{ft} + \upsilon_{f}\right)\frac{\partial \overline{w}^{f}}{\partial z} \tag{3.14}$$

It is noted from the continuity equation that the divergence of the fluid phase velocity is not zero; therefore the second term in the above equations is non-trivial. The kinematic viscosity of the fluid is υ_{f}, the fluid phase eddy viscosity is υ_{ft} and k_{f} is the fluid phase turbulent kinetic energy given by

$$k_{f} = \frac{1}{2\left(1-\overline{c}\right)}\left(1-c\right)\Delta u_{i}{}^{f}\Delta u_{i}{}^{f} \tag{3.15}$$

The fluid phase eddy viscosity is given by,

$$\upsilon_{ft} = C_\mu \frac{{k_f}^2 (1-\bar{c})}{\varepsilon_f} \tag{3.16}$$

In which C_μ is an empirical coefficient and the fluid phase turbulent energy dissipation rate is given by

$$\varepsilon_f = \frac{1}{\rho^f (1-\bar{c})} (1-c) \tau_{ij}^f \frac{\partial \Delta {u_i}^f}{\partial x_j} \tag{3.17}$$

The balance equation for the turbulent kinetic energy k_f and the turbulent energy dissipation rate ε_f is given by

$$\begin{aligned} \frac{\partial}{\partial t} \rho^f (1-\bar{c}) k_f = & -\frac{\partial}{\partial z} \rho^f (1-\bar{c}) k_f \overline{w}^f + \tau_{xz}^{ft} \frac{\partial \overline{u}^f}{\partial z} \\ & + \tau_{zz}^{ft} \frac{\partial \overline{w}^f}{\partial z} + \frac{\partial}{\partial z} \left[\left(\upsilon + \frac{\upsilon_{ft}}{\sigma_k} \right) \frac{\partial \rho^f (1-\bar{c}) k_f}{\partial z} \right] \\ & - (1-\bar{c}) \rho^f \varepsilon_f + \beta \upsilon_{ft} \frac{\partial \bar{c}}{\partial z} \left(\overline{w}^f - \overline{w}^s \right) - 2 \rho^s \bar{c} k_f \beta (1-\alpha) \end{aligned} \tag{3.18}$$

The first term on the right hand side is the advection term. The second and the third terms represent the production of kinetic energy or turbulence. The fourth term indicates the turbulent diffusion term. The next term represents turbulent or viscous dissipation followed by dissipation due to the turbulent suspension. The last term, which basically involves the correlation between fluid and sediment velocity fluctuations, represents the dissipation of turbulent energy where α is a measure of the degree of correlation. The particle response time is given as the time taken for a particle at rest to accelerate to the velocity of the surrounding fluid. From Drew (1976) this time t_p is given by

$$t_p \equiv \frac{\rho^s}{\beta} \tag{3.19}$$

The time between collisions t_c is calculated based on the mean free path l_c of the colliding particles and the strength of the sediment velocity fluctuations $k_s^{1/2}$

$$t_c = \frac{l_c}{k_s^{1/2}} \tag{3.20}$$

The length scale l_c is defined by

$$l_c = \frac{\sqrt{\pi}d}{24\bar{c}g_0(\bar{c})} \tag{3.21}$$

The definition of $g_0(\bar{c})$, the contact value of the radial distribution function, is given in the next section.

Based on the above definitions, the parameter α is found to be dependent on the relative magnitudes of the particle response time t_p and the fluid turbulence time scale t_l which is given by Elghobashi and Abou-Arab (1983) as

$$t_l \equiv 0.165\frac{k_f}{\varepsilon_f} \tag{3.22}$$

Additionally, α in equation (3.18) also depends on the time between collisions t_c and is given by

$$\alpha = \left(1 + \frac{t_p}{\min(t_l, t_c)}\right)^{-1} \tag{3.23}$$

The balance equation for the turbulent energy dissipation is given from Elghobashi and Abou-Arab (1983) as

$$\frac{\partial}{\partial t}\rho^f(1-\bar{c})\varepsilon_f = -\frac{\partial}{\partial z}\rho^f(1-\bar{c})\varepsilon_f\overline{w}^f + C_{\varepsilon 1}\frac{\varepsilon_f}{k_f}\left(\tau^{ft}{}_{xz}\frac{\partial\overline{u}^f}{\partial z} + \tau^{ft}{}_{zz}\frac{\partial\overline{w}^f}{\partial z}\right)$$
$$+\frac{\partial}{\partial z}\left[\left(\upsilon + \frac{\upsilon_{ft}}{\sigma_\varepsilon}\right)\frac{\partial\rho^f(1-\bar{c})\varepsilon_f}{\partial z}\right] - C_{\varepsilon 2}\frac{\varepsilon_f}{k_f}(1-\bar{c})\rho^f\varepsilon_f$$
$$-C_{\varepsilon 3}\frac{\varepsilon_f}{k_f}2\rho^s\bar{c}k_f\beta(1-\alpha) + C_{\varepsilon 3}\frac{\varepsilon_f}{k_f}\beta\upsilon_{ft}\frac{\partial\bar{c}}{\partial z}\left(\overline{w}^f - \overline{w}^s\right) \tag{3.24}$$

In the absence of appropriate values for the coefficients in the $k_f - \varepsilon_f$, numerical values for the clear fluid from the $k-\varepsilon$ taken from Rodi (1984) are used. In the above balance equation, if the averaged sediment concentration is set to zero the standard $k-\varepsilon$ equation for a clear fluid is obtained. The set of the numerical coefficients used in this particular equation is given in table 3.1

Table 3.1 Summary of numerical coefficients adopted by the model

C_μ	$C_{\varepsilon 1}$	$C_{\varepsilon 2}$	$C_{\varepsilon 3}$	σ_k	σ_ε	C_s	σ_s
0.09	1.44	1.92	1.2	1.0	1.3	0.55	1.0

3.4 Closure of Sediment Stress

3.4.1 Sediment Transport Equation

Like the fluid stresses, the sediment stress can be written down in terms of the sum of the small-scale particles stress and the large-scale Reynolds stress

$$\tau^s_{xz} = \tau^{s0}_{xz} + R^s_{xz}; \qquad \tau^s_{zz} = \tau^{s0}_{zz} + R^s_{zz} \tag{3.25}$$

The small-scale stresses are due to inter-particle interactions resulting from collisions or interstitial fluid effects. The large-scale Reynolds stresses are due to sediment velocity fluctuations and associated concentration fluctuations given as

$$R_{xz}^{s} = -\rho^{s} c \Delta u^{s} \Delta w^{s} \; ; \qquad R_{zz}^{s} = -\rho^{s} c \Delta w^{s} \Delta w^{s} \tag{3.26}$$

The sediment fluctuation energy, which is analogous to the fluid-phase turbulent kinetic energy, is given as

$$k_{s} \equiv \frac{1}{2\bar{c}} c \Delta u_{i}{}^{s} \Delta u_{i}{}^{s} \tag{3.27}$$

Since this closure method is more suitable to the large-scale stresses, it is assumed that this closure can describe sediment fluctuations even at the small-scale and in the small-scale limit we let $\Delta u_{i}{}^{s} = u_{i}^{s''}$, where $u_{i}^{s''}$ represents the small-scale velocity. However, at small scales concentration fluctuations are absent, and as a result the fluctuating part of the concentration is ignored. Accordingly, the concentration is the mean value obtained from the averaging process. Therefore the above sediment-phase turbulent kinetic energy can be written as

$$k_{s} \equiv \frac{1}{2} u_{i}^{s''} u_{i}^{s''} \tag{3.28}$$

The concept of granular temperature is introduced from Nott and Brady (1994) and Jenkins and Hanes (1998) and the above equation is written as

$$T_{s} = \frac{1}{3} \left\langle u_{i}^{s''} u_{i}^{s''} \right\rangle \tag{3.29}$$

Where the brackets denote ensemble averaging. Analogous to the fluid phase turbulent energy, the sediment fluctuation energy, which is the turbulent kinetic energy counterpart for the solids phase, can be derived from sediment-phase momentum equation. The small-scale granular temperature and the sediment fluctuation energy are coupled together to provide a single transport equation as follows from Hsu (2002)

$$\rho^s\left(\frac{\partial \bar{c}K_s}{\partial t}+\frac{\partial \bar{c}K_s\overline{w}^s}{\partial z}\right)=\tau_{xz}^s\frac{\partial \overline{u}^s}{\partial z}+\tau_{zz}^s\frac{\partial \overline{w}^s}{\partial z}-\frac{\partial Q}{\partial z}-\gamma+2\beta\bar{c}\left(\alpha k_f-K_s\right) \tag{3.30}$$

Where Q denotes the sediment fluctuation energy flux and γ is the rate of energy dissipation. The total sediment stress is used to encompass the small-scale and the large-scale stresses. The last term in the above equation is similar to the last term of the fluid phase turbulent kinetic energy and describes the interaction between the two phases. This can be written down as two terms. One term is the fluid turbulent kinetic energy $2\beta\bar{c}\,\alpha k_f$ associated with the turbulent eddies acting on the random sediment particles and thereby enhancing the sediment fluctuation energy. The other term is associated with the drag due to the interstitial fluid and additional dissipation mechanism present in the form $2\beta\bar{c}K_s$.

The above equation would need further closures to solve the transport equation in terms of the sediment stresses, flux of the fluctuating energy, and energy dissipation. Let the flux of the sediment fluctuation energy Q be the sum of the small scale Q_0 and the large scale Q_1 components. Therefore,

$$Q=Q_0+Q_1 \tag{3.31}$$

and energy dissipation is taken to be collisional dissipation associated with the inelasticity of particles as explained next.

3.4.2 Collisional Theory of Granular Flow

Following Jenkins and Hanes (1998) the closure for the small-scale inter-granular stresses is given by the kinetic theory of collisional granular flow. This theory is an extension of the classical kinetic theory applied to dense particle flow and provides explicit closures to dissipation due to the inelastic particle-particle collisions by introducing a coefficient of

restitution. The assumption made in theory is that the normal stress τ_{zz}^{s} is function of the sediment concentration, sediment properties and sediment fluctuation energy. Therefore,

$$\tau_{zz}^{s0} = -\frac{2}{3}\rho^{s}\bar{c}(1+4G)K_{s} + AE\frac{\partial\overline{w}^{s}}{\partial z} \tag{3.32}$$

where $G = \bar{c}g_0(\bar{c})$, AE, which is the product of A and E, is the sediment viscosity due to collisions and $g_0(\bar{c})$ is a radial distribution function at contact for identical spheres, provided by the following expression from Torquato (1995)

$$g_0(\bar{c}) = \begin{cases} \dfrac{(2-\bar{c})}{2(2-\bar{c})^3} & 0 < \bar{c} < 0.49 \\ \dfrac{0.8537}{(0.64-\bar{c})^{p}} & 0.49 \le \bar{c} \le 0.635 \end{cases} \tag{3.33}$$

In the above equation, p=1. The particle collisional shear stress is given by

$$\tau_{xz}^{s0} = AE\frac{\partial\overline{u}^{s}}{\partial z} \tag{3.34}$$

where, from Jenkins and Hanes (1998)

$$A = 8d\rho^{s}\bar{c}G\left(\frac{2}{3}K_{s}\right)^{1/2} \quad ; \qquad E = 1+\frac{\pi}{12}\left(1+\frac{5}{8G}\right)^{2} \tag{3.35}$$

and,

$$Q_0 = -\frac{5}{3}AM\frac{\partial K_{s}}{\partial z} \qquad\qquad M = 1+\frac{9\pi}{32}\left(1+\frac{5\pi}{12G}\right)^{2} \tag{3.36}$$

Finally the rate of dissipation is closed as follows from Jenkins and Savage (1983),

$$\gamma = \left(\frac{10A}{d^{2}} - 4\rho^{s}\bar{c}G\frac{\partial\overline{w}^{s}}{\partial z}\right)(1-e)K_{s} \tag{3.37}$$

The coefficient of restitution *e* is taken as 0.8. It should be noted that *e* represents the ratio of the velocities before and after an impact. For a completely elastic collision *e*=1and for completely inelastic collision *e*=0.

3.4.3 Large Scale Sediment Stress

The large scale sediment stresses are closed using the eddy viscosity model. The shear stress is closed as

$$R_{xz}^{s} = \rho^{s} \upsilon_{st} \frac{\partial \widetilde{u}^{s}}{\partial z} \tag{3.38}$$

and the normal stress as

$$R_{xz}^{s} = -\frac{2}{3}\rho^{s}\bar{c}K_{s} + \frac{4}{3}\rho^{s}\upsilon_{st}\frac{\partial \widetilde{w}^{s}}{\partial z} \tag{3.39}$$

The sediment viscosity is connected to the sediment fluctuation energy through the sediment mixing length l_s ,

$$\upsilon_{st} = C_{s}\bar{c}l_{s}\sqrt{K_{s}} \tag{3.40}$$

where C_s = 0.55.The sediment mixing length is connected to the turbulent fluid flow mixing length, as the large scale velocity and concentration fluctuations are caused by turbulence through the factor α as follows ,

$$l_{s} = \alpha l_{f} \tag{3.41}$$

If the particles are large, then the particle response time is large, indicating that the turbulent eddies do not contribute to the sediment velocity fluctuation, which in turn would mean that $\alpha \approx 0$. If the particles are fine, then the particle response time will be small, indicating that turbulence does play a role in the sediment velocity fluctuation. In that case $\alpha \approx 1$ and the

sediment mixing length is nearly equal to the turbulent mixing length. The turbulent mixing length is given by,

$$l_f = 0.165 \frac{k_f^{3/2}}{\varepsilon_f} \tag{3.42}$$

The energy flux due to large-scale sediment fluctuations is given by

$$Q_1 = -\rho^s \frac{\upsilon_{st}}{\sigma_s} \frac{\partial K_s}{\partial z} \tag{3.43}$$

where σ_s is taken to be 1 for simplicity.

3.4.4 Closure at Low Concentrations

The theory of gases, which is used as an analogy for the collisional granular flow theory, would not be a good assumption when the suspension is dilute. Sediment concentration becomes dilute near the flow surface and collisions among particles become infrequent, which violates an important postulate of the kinetic theory for it to remain statically valid. In such a scenario fluid turbulence acts as a major cause of sediment suspension. As turbulence gives rise to large-scale Reynolds stresses, the small-scale dilute suspension stresses τ_{xz}^{s0} and τ_{zz}^{s0} must be closed appropriately. For this a damping parameter δ is introduced in terms of the mean free path l_c and the turbulence mixing length l_f ,

$$\delta = \frac{l_f}{l_f + l_c} \tag{3.44}$$

If the mean free path increases then the sediment is diluting further and the small-scale stresses keep decreasing by the factor δ . Using δ and from equations (3.25), (3.34), (3.38) and (3.44) the total shear stress is

$$\tau_{xz}^{s} = \delta\tau_{xz}^{s0} + R_{xz}^{s} = \left(\delta AE + \rho^{s}\upsilon_{st}\right)\frac{\partial\widetilde{u}^{s}}{\partial z} \tag{3.45}$$

and the normal stress is

$$\tau_{zz}^{s} = \delta\tau_{zz}^{s0} + R_{zz}^{s} = -\frac{2}{3}\rho^{s}\bar{c}\left[\left(1+4G\right)\delta+1\right]K_{s} + \left(\delta AE + \frac{4}{3}\rho^{s}\upsilon_{st}\right)\frac{\partial\widetilde{w}^{s}}{\partial z} \tag{3.46}$$

Thus the energy flux is given by

$$Q = Q_0 + Q_1 = -\left(\frac{5}{3}AM\delta + \rho^{s}\frac{\upsilon_{st}}{\sigma_{s}}\right)\frac{\partial K_{s}}{\partial z} \tag{3.47}$$

3.4.5 Region of Enduring Contact

The kinetic theory of granular flow can be applied when the concentrations are low so that the time for inter-particle collision, *i*, short and in conformity with the kinetic theory of gases. However, when the concentration is higher the collision time will not be short, as there will be enduring contacts between the particles. Therefore kinetic theory can no longer be applied. In between random loose packing c_* and random close packing c^* sediment behaves in a transitional way from having fluid-like properties to having solid-like behavior.

As the concentration increases the collisional contribution of the particle normal stress decreases because shearing reduces between the particles and the fluctuations become very small. However, the contribution from enduring contacts increases the normal stress. Therefore it may be assumed that the particle normal stress is a sum of the collisional normal stress and normal stress due to enduring contact:

$$\tau_{zz}^{s} = \tau_{zz}^{sc} + \tau_{zz}^{se} \tag{3.48}$$

The collisional normal stress is closed using equation (2.32), whereas for the normal stress due to enduring contacts, a Hertz contact relation is used and given as

$$\tau_{zz}^{se} = \frac{m}{\pi d^2} K \bar{c} \left(\frac{\Delta}{d} \right)^{3/2} \tag{3.49}$$

where Δ is the average compressive volume strain, K is the average number of contacts per particle or coordination number and m is given as follows,

$$m = \frac{2}{9\sqrt{3}} \frac{\mu_e d^2}{1-\upsilon} \tag{3.50}$$

where μ_e is the shear modulus and υ is Poisson's ratio. The ratio of $\frac{\Delta}{d}$ is related to the concentration difference as follows,

$$\frac{\Delta}{d} = \left(\bar{c} - c_* \right)^{2\chi/3} \tag{3.51}$$

Therefore from the above equations,

$$\tau_{zz}^{se} = \begin{cases} 0 & \bar{c} < c_* \\ \dfrac{m}{\pi d^2} K(\bar{c}) \bar{c} (\bar{c} - c_*)^{\chi} & c_* \le \bar{c} \le c^* \end{cases} \tag{3.52}$$

and the coordination number K is taken to be a function of concentration,

$$K(\bar{c}) = 3 + 3\sin\left[\frac{\pi}{2} \left(2 \frac{\bar{c} - c_*}{c^* - c_*} - 1 \right) \right] \qquad c_* \le \bar{c} \le c^* \tag{3.53}$$

3.5 Initial and Boundary Conditions

3.5.1 Initial Condition

The sediment bed, when agitated by turbulent flow, is disturbed from the it's stationary position and the granules are entrained .They either are kept suspended and move along with turbulent motion or settle down and exchange momentum with other stationary particles and

attempt to dislodge them. This process of sediment transport and its initiation cannot be studied by examining the interaction process of every individual particle. Therefore, in order to initialize sediment motion an assumed sediment profile $\bar{c}_{ini}(z)$ is used as the initial condition. The maximum concentration c^* is taken at the bed and may simply be assumed to decrease linearly to a concentration of 0.4 at about half the water depth. Initially the fluid and sediment phase velocities are considered to be zero, i.e. $\widetilde{u}^f = \widetilde{u}^s = 0$ and $\widetilde{w}^f = \widetilde{w}^s = 0$ from Hsu (2002). To accelerate the computations the sediment vertical velocity is set to zero and the flow is calculated up to an initial time T_0, which is taken to be 10 times the turnover time $t_{L0} = \frac{h}{u*}$ of the largest eddy with *h* being the water depth. After time T_0 the vertical motion of sediment is calculated using the sediment momentum equation.

3.5.2 Bottom Boundary Condition

The bottom boundary condition for the sediment phase is applied at the interface where the porous stationary part of the sediment bed fails, the sediment is sheared and the granular bed is fluidized leading to the formation of a region where the bed moves slowly creating a condition conducive to enduring contacts among particles. If the concentration of particles is larger than the random close-packed concentration c_*, then fluidizing the particles would not be possible; therefore a failure concentration $\widehat{c}$ is defined as the concentration at which the particles are first sheared. The applied external shear can result in erosion or settling and accumulation on the bed.

In the porous stationary bed layer, the sediment horizontal velocity $\widetilde{u}_s$, the vertical velocity $\widetilde{w}_s$, and the sediment fluctuation energy k_s, disappear, giving rise to the condition in the stationary bed

$$\widetilde{u}_s = 0 \qquad \widetilde{w}_s = 0 \qquad k_s = 0 \tag{3.54}$$

The bed location, which depends on the external shear and changes according to the external flow conditions, is determined as part of the solution. The failure concentration is given by the Coulomb failure criterion as

$$\tau_{xz}^{s} = \tau_{zz}^{s} \tan\phi \tag{3.55}$$

where ϕ is the angle of friction of the sediment. Therefore, from equations (3.48) and (3.52) and (3.55)

$$K\bar{c}\left(\bar{c} - c_{*}\right)^{n} = \frac{\pi d^{2}}{m}\left(\frac{\tau_{xz}^{s}}{\tan\phi} - \tau_{xz}^{sc}\right) \tag{3.56}$$

Along with the implementation of the boundary conditions given in (3.54), τ_{xz}^{s} and τ_{xz}^{sc} are obtained from their closures, and solving the above non-linear equation (3.56) the failure concentration $\widehat{c}$ is obtained. At this point the bed is set in motion and its location is specified. The stress τ_{xz}^{s} changes with the external flow condition indicating that $\widehat{c}$ and the bed location also vary along with external flow.

3.5.3 Top Boundary Condition

Fluid Phase: The top boundary is considered to be a rigid hydraulically smooth lid. In a fully developed turbulent flow the horizontal velocity profile is assumed to follow the logarithmic law of the wall given as

$$\frac{\widetilde{u}^{f}}{u_{*t}} = \frac{1}{\kappa}\ln\left[\frac{9u_{*t}}{\nu_{f}}z\right] \tag{3.57}$$

where the von Karman constant κ in the sediment-laden flow is taken as 0.41and u_{*_t} is the friction velocity at the top of the rigid lid (Hsu, 2002). Given the fluid velocity calculated in the

flow domain near the top lid the friction velocity can be found and the horizontal velocity gradient at the rigid lid is given as

$$\frac{\partial \tilde{u}^f}{\partial z} = \frac{u_{*_t}}{\nu_f} \tag{3.58}$$

The vertical fluid velocity at the top of the boundary $\tilde{w}^f = 0$ .The no-flux boundary condition with respect to the turbulent kinetic energy is used for the top boundary condition

$$\frac{\partial k_f}{\partial z} = 0 \tag{3.59}$$

The turbulent energy dissipation rate ε_f is specified based on the assumption that production equals dissipation in the logarithmic region:

$$\varepsilon_f = \frac{C_\mu^{3/4} k_f^{3/2}}{\kappa z} \tag{3.60}$$

It is noted from equation 3.18 that there are two more terms that are responsible for dissipation like dissipation due to drag and dissipation due to turbulent suspension flux. Hence it is not steady-state turbulence.

The Neumann boundary-conditions are applied to the lateral and bottom fluid pressures, and $\overline{\mathrm{P}}^f = 0$ is applied to the top boundary as a reference pressure.

Sediment phase: At the top the sediment concentration is usually zero or dilute. In the present model the top of the sediment phase is considered to be the interface at which the sediment concentration becomes less than a specified concentration of $c_{\min}$. Above this interface the concentration is considered to be zero. The calculations (next chapter) are insensitive to $c_{\min}$ as long as it is small. In the present case $c_{\min}$ has been taken to be $c_{\min} = 5 \times 10^{-4}$.

The horizontal velocity of the sediment phase has a free slip velocity at the top boundary

$$\frac{\partial \overline{u}^s}{\partial z} = 0 \tag{3.61}$$

indicating that the sediment shear stress is negligible for low sediment concentration at the top boundary. It should be noted that this boundary is not the lid but where $c_{\min}$ is defined. Similarly the no-flux condition is applied to the sediment fluctuation energy at the top boundary for the sediment phase,

$$\frac{\partial k_s}{\partial z} = 0 \tag{3.62}$$

The location of the top boundary of sediment changes according to the external conditions similar to the porous stationary bed. The sediment concentration and the vertical velocity are considered to be zero above the top boundary.

3.5.4 Lateral Boundary Condition

The flow is driven by a horizontal pressure gradient. In experiments that involve steady flow in an open channel, the flow is driven by gravity through the horizontal momentum equation. In the present case the gravity term in the fluid momentum equation is converted to the horizontal pressure gradient term .Therefore for the steady gravity driven flow with a given slope S or a frictional velocity u_* and hydraulic radius r_b, the horizontal pressure gradient is given as

$$\frac{1}{\rho^f}\frac{\partial \overline{P}^f}{\partial x} = gS = -\frac{u_*^2}{r_b} \tag{3.63}$$

CHAPTER 4
NUMERICAL IMPLEMENTATION

4.1 Introduction

The fluid and sediment phase continuity equations (3.1) and (3.2) along with the momentum equations (3.3), (3.4), (3.9) and (3.10) define the dynamics of the system to be examined. The turbulent kinetic energy balance equation (3.18) and the balance equation for turbulent energy dissipation rate (3.24) along with the sediment phase fluctuation energy balance equation (3.30) are solved numerically using a finite difference scheme. The implementation scheme is described in this chapter.

4.2 Mesh and Grid System

The mesh formed for the computational domain is implemented using the staggered-grid approach. In this the fluid horizontal velocity $\widetilde{u}^f$, the sediment horizontal velocity $\widetilde{u}^s$, fluid pressure $\overline{P}^f$, sediment concentration $\overline{c}$, fluid turbulence kinetic energy k_f, the turbulent energy dissipation rate ε_f, and the sediment fluctuation energy k_s are calculated at the center of the grid while the sediment phase vertical velocity $\widetilde{w}^s$, and the fluid phase vertical velocity $\widetilde{w}^f$ are taken at the top face of the grid.

The quantities do not vary in the downslope (x) direction; i.e. a uniform flow is assumed. Variations in the z-direction are solved for. The computational domain is discretized into N+2 grids with single ghost grids at the top and the bottom. As mentioned previously, the flow is driven through a horizontal pressure gradient $\partial\overline{P}^f / \partial x$ and to facilitate these two columns of ghost grids are specified to allow implementation of the pressure gradient. Since only a vertical column in considered for the calculations, the ghost grids help in setting up the problem by letting flow develop in the pseudo sense in the horizontal direction.

4.3 Numerical Discretization

A modified two-step projection method is used to solve the two-phase equations. The numerical scheme proceeds by first discretizing the sediment phase continuity and momentum equations and the necessary sediment phase values like $\bar{c}$, $\tilde{u}^s$, $\tilde{w}^s$ and k_s are obtained by the predictor-corrector method .Once these values are updated at a new time level, the fluid phase mass and momentum equations are solved again using the predictor-corrector method. With these values solved for, after every computational cycle, the k_f and ε_f equations are solved and updated.

4.3.1 Solution of Sediment Phase Equations

The values of $\tilde{u}^s$, $\tilde{w}^s$ and k_s are not directly solved from the governing equations; instead, the following sediment phase variable definitions are introduced.

The sediment horizontal momentum per unit mass given as

$$U = \rho^s \bar{c} \tilde{u}^s \tag{4.1}$$

Next, the sediment vertical momentum per unit mass is

$$W = \rho^s \bar{c} \tilde{w}^s \tag{4.2}$$

and from the sediment fluctuation energy equation, the fluctuation energy per unit mass, or specific fluctuation energy, is given as

$$K = \rho^s \bar{c} k_s \tag{4.3}$$

These definitions help avoid any singularities in the governing equations as the concentration approaches zero. Based on the calculated values of $\bar{c}$, U, W and K, the predictor-corrector scheme is described next.

4.3.1.1 Predictor Step

The forward time difference method is used to discretize the time derivative. Initially there is a predictor step in which at a new time-step (n) the sediment phase variables, $\bar{c}, U, W, K$ are calculated from the known values at the previous time step (n-1). Let j denote the grid index in the z-direction. The sediment phase continuity equation (3.2) is discretized in the predictor scheme as follows

$$\hat{\bar{c}} = \bar{c}_j^{(n-1)} + \frac{\Delta t}{\rho^s} RHSC_j^{(n-1)} \tag{4.4}$$

where $\hat{\bar{c}}$ indicates the tentative sediment concentration at time-step n and $RHSC$ indicates the right-hand sediment concentration in terms of sediment vertical momentum per unit mass given as

$$RHSC_j^{(n-1)} = \frac{W_{j+1/2}^{(n-1)} - W_{j-1/2}^{(n-1)}}{\Delta z_j} \tag{4.5}$$

From equation (3.9) the sediment horizontal momentum equation per unit mass is given as follows

$$\hat{U}_j = \frac{U_j^{(n-1)} + RHSU_j^{(n-1)} \Delta t}{1 + \beta_j^{(n-1)} \Delta t} \tag{4.6}$$

where β is defined in equation 3.5 and $RHSU_j^{(n-1)}$ is given as

$$RHSU_j^{(n-1)} = \left[CVX + STX - \rho^s Sg\bar{c} + \beta \bar{c}\tilde{u} f \right]_j^{(n-1)} \tag{4.7}$$

and CVX stands for the advection term in the x-direction. When compared to equation (3.9) it is denoted as

$$CVX = -\left(\frac{\partial U \widetilde{w}^{s}}{\partial z} \right) \tag{4.8}$$

This term is discretized with a central difference scheme around the point j as follows

$$CVX_j = -\left(\frac{\partial U \widetilde{w}^{s}}{\partial z} \right)_j = \frac{U_{j+1/2} \widetilde{w}^{s}_{j+1/2} - U_{j-1/2} \widetilde{w}^{s}_{j-1/2}}{\Delta z_j} \tag{4.9}$$

STX in equation (4.7) stands for the stress term in the horizontal direction and is given as

$$STX = \left(\frac{\partial \tau^{s}_{xz}}{\partial z} \right) \tag{4.10}$$

This term is centered on point j and is discretized as follows:

$$STX_j = \left(\frac{\partial \tau^{s}_{xz}}{\partial z} \right)_j = \frac{\left(\tau^{s}_{xz} \right)_{j+1/2} - \left(\tau^{s}_{xz} \right)_{j-1/2}}{\Delta z_j} \tag{4.11}$$

$U_{j+1/2}$ in equation (4.9) is based on a combination of central and upwind scheme given as

$$U_{j+1/2} = \frac{1}{2}\left[1 + \varphi SIG\left(\widetilde{w}^{s}_{j+1/2}\right)\right]U_j + \frac{1}{2}\left[1 - \varphi SIG\left(\widetilde{w}^{s}_{j+1/2}\right)\right]U_{j+1} \tag{4.12}$$

which $SIG(\ )$ is the sign function which depends on the direction of the vertical velocity and φ is a numerical coefficient taken to be 1 for upwind and 0 for a central difference scheme in the present model.

In equation (4.12)

$$\widetilde{w}^{s}_{j+1} = \frac{\widetilde{w}^{s}_{j+3/2} + \widetilde{w}^{s}_{j+1/2}}{2} \tag{4.13}$$

From the vertical sediment momentum equation (3.10), the vertical specific momentum is given as

$$\hat{W}_{j+1/2} = \frac{W_{j+1/2}^{(n-1)} + RHSW_{j+1/2}^{(n-1)}\Delta t}{1+\beta_{j+1/2}^{(n-1)}\Delta t} \tag{4.14}$$

Note the difference in the vertical grid index. This is as a result of the staggered grid where the sediment horizontal and vertical velocities are calculated at different grid points. In the above equation $RHSW_{j+1/2}^{(n-1)}$ is given by

$$RHSW_{j+1/2}^{(n-1)} = \left[CVZ + STZ + PF + TS - \rho^s g\bar{c} + \left(\beta\bar{c}\tilde{w}^f\right)\right]_{j+1/2}^{(n-1)} \tag{4.15}$$

and similar to the horizontal momentum equation, CVZ represents the convection term in the z-direction and given as

$$CVZ = -\left(\frac{\partial W\tilde{w}^s}{\partial z}\right) \tag{4.16}$$

Centered on grid index j+1/2, the vertical convection term is discretized as follows:

$$CVZ_{j+1/2} = -\left(\frac{\partial W\tilde{w}^s}{\partial z}\right)_{j+1/2} = \frac{W_{j+1}\tilde{w}^s_{j+1} - W_j\tilde{w}^s_j}{(\Delta z_j + \Delta z_{j+1})/2} \tag{4.17}$$

STZ in equation (4.15) is the stress in the vertical direction,

$$STZ = \left(\frac{\partial \tau^s_{zz}}{\partial z}\right) \tag{4.18}$$

This term is calculated as

$$STZ_{j+1/2} = \left(\frac{\partial \tau_{zz}^{s}}{\partial z} \right)_{j+1/2} = \frac{\left(\tau_{zz}^{s} \right)_{j+1} - \left(\tau_{zz}^{s} \right)_{j-1/2}}{(\Delta z_j + \Delta z_{j+1})/2} \tag{4.19}$$

PF in equation (4.15) is the pressure term,

$$PF = -\left(\overline{c} \frac{\partial \overline{P}^{f}}{\partial z} \right) \tag{4.20}$$

and is discretized as

$$PF_{j+1/2} = -\left(\overline{c} \frac{\partial \overline{P}^{f}}{\partial z} \right)_{j+1/2} = -\overline{c}_{j+1/2} \frac{\overline{P}_{j+1}^{f} - \overline{P}_{j}^{f}}{(\Delta z_j + \Delta z_{j+1})/2} \tag{4.21}$$

$\overline{c}_{j+1/2}$ in the above equation is obtained as linear interpolation

$$\overline{c}_{j+1/2} = \frac{\Delta z_j \overline{c}_{j+1} + \Delta z_{j+1} \overline{c}_j}{\Delta z_j + \Delta z_{j+1}} \tag{4.22}$$

and TS is the turbulent suspension flux term in the vertical direction

$$TS = -\left(\beta \upsilon_{ft} \frac{\partial \overline{c}}{\partial z} \right) \tag{4.23}$$

This term is calculated as

$$TS_{j+1/2} = -\left(\beta \upsilon_{ft} \frac{\partial \overline{c}}{\partial z} \right)_{j+1/2} = -\beta_{j+1/2} \left(\upsilon_{ft} \right)_{j+1/2} \frac{\overline{c}_{j+1} - \overline{c}_j}{(\Delta z_j + \Delta z_{j+1})/2} \tag{4.24}$$

With a linear interpolation of the fluid eddy viscosity

$$\left(\upsilon_{ft} \right)_{j+1/2} = \frac{\Delta z_j \left(\upsilon_{ft} \right)_{j+1} + \Delta z_{j+1} \left(\upsilon_{ft} \right)_j}{\Delta z_j + \Delta z_{j+1}} \tag{4.25}$$

For the above equations, W_{j+1} is given by a combination of the central and the upwind scheme as follows:

$$W_{j+1} = \frac{1}{2}\left[1 + \varphi SIG\left(\tilde{w}^s_{j+1/2}\right)\right]W_{j+1/2} + \frac{1}{2}\left[1 - \varphi SIG\left(\tilde{w}^s_{j+1/2}\right)\right]U_{j+3/2} \tag{4.26}$$

Similarly, from sediment fluctuation energy equation (3.30), the specific fluctuation energy is given by

$$\hat{K}_j = \frac{K_j^{(n-1)} + RHSK_j^{(n-1)}\Delta t}{1 + \left[2\beta + \gamma_0\right]_j^{(n-1)}\Delta t} \tag{4.27}$$

γ_0 being part of the collisional dissipation term equation (3.37) in the absence of *K*, and where

$$RHSK_j^{(n-1)} = \left[CVK + PROD + DIF + 2\beta\overline{c}\,\alpha k_f\right]_j^{(n-1)} \tag{4.28}$$

Where α is defined in equation (3.23) and CVK being the convection term,

$$CVK = -\left(\frac{\partial K\tilde{w}^s}{\partial z}\right) \tag{4.29}$$

This term is calculated similarly to convection term in equation (4.9) and is given as

$$CVK_j = -\left(\frac{\partial UK}{\partial z}\right)_j = \frac{K_{j+1/2}\tilde{w}^s_{j+1/2} - K_{j-1/2}\tilde{w}^s_{j-1/2}}{\Delta z_j} \tag{4.30}$$

$PROD$ in equation (4.28) is the production term,

$$PROD = \left(\tau^s_{xz}\frac{\partial\tilde{u}^s}{\partial z} + \tau^s_{zz}\frac{\partial\tilde{w}^s}{\partial z}\right) \tag{4.31}$$

This term is calculated as

$$
\begin{aligned}
PROD_j &= \left(\tau_{xz}^s \frac{\partial \tilde{u}^s}{\partial z} + \tau_{zz}^s \frac{\partial \tilde{w}^s}{\partial z} \right) \\
&= \left(\tau_{xz}^s\right)_j \frac{\left(\frac{\partial \tilde{u}^s}{\partial z}\right)_{j+1/2} + \left(\frac{\partial \tilde{u}^s}{\partial z}\right)_{j-1/2}}{2} \\
&+ \left(\tau_{zz}^s\right)_j \frac{\left(\frac{\partial \tilde{w}^s}{\partial z}\right)_{j+1/2} + \left(\frac{\partial \tilde{w}^s}{\partial z}\right)_{j-1/2}}{2}
\end{aligned}
\tag{4.32}
$$

The terms $(\tau_{xz}^s)_j$, $(\partial \tilde{u}^s / \partial z)_{j+1/2}$ and $(\partial \tilde{u}^s / \partial z)_{j-1/2}$ can be obtained from interpolation as shown previously.

The diffusion term *DIF* in equation 4.28 is defined as

$$
DIF = -\frac{\partial Q}{\partial z} \tag{4.33}
$$

This term is calculated similarly to the stress term in the *x*-direction as given in equation (4.11) according to

$$
DIF_j = -\left(\frac{\partial Q}{\partial z}\right)_j = -\frac{Q_{j+1/2} - Q_{j-1/2}}{\Delta z_j} \tag{4.34}
$$

Similar to equations (4.12) and (4.26) , $K_{j+1/2}$ is given as

$$
K_{j+1/2} = \frac{1}{2}\left[1 + \varphi SIG\left(\tilde{w}_{j+1/2}^s\right)\right] K_j + \frac{1}{2}\left[1 - \varphi SIG\left(\tilde{w}_{j+1/2}^s\right)\right] K_{j+1} \tag{4.35}
$$

In the same way, $U_{j-1/2}$, W_j, $K_{j-1/2}$ are obtained similarly to equations (4.12), (4.26), (4.35).

4.3.1.2 Corrector Step

In the corrector step the predicted value of the time derivative is obtained at the next time step by substituting the newly obtained predicted values of $\hat{\bar{c}}_j$, $\hat{U}_j$, $\hat{W}_{j+1/2}$, $\hat{K}_j$ and calculate $\widehat{RHSC}_j$, $\widehat{RHSU}_j$, $\widehat{RHSW}_j$ and $\widehat{RHSK}_j$. These quantities are obtained from

$$\widehat{RHSC}_j = \frac{\hat{W}_{j+1/2} - \hat{W}_{j-1/2}}{\Delta z_j} \tag{4.36}$$

$$\widehat{RHSU}_j = \left[\widehat{CVX} + \widehat{STX} - \rho^s S g \hat{\bar{c}} + \left(\beta \bar{c} \tilde{u}^f \right)^{(n-1)} \right]_j \tag{4.37}$$

$$\widehat{RHSW}_j = \left[\widehat{SVZ} + \widehat{STZ} + \widehat{PF} + \widehat{TS} - \rho^s g \hat{\bar{c}} + \left(\beta \bar{c} \tilde{w}^f \right)^{(n-1)} \right]_{j+1/2} \tag{4.38}$$

and

$$\widehat{RHSK}_j = \left[\widehat{CVK} + \widehat{PROD} + \widehat{DIF} + 2\beta \bar{c} \alpha k_f^{(n-1)} \right]_j \tag{4.39}$$

All the terms on the right hand sides of equations (4.36) to (4.39) with a circumflex (cap) denote the same corresponding quantities as explained earlier in the predictor step but are calculated using the newly obtained values of $\hat{\bar{c}}_j$, $\hat{U}_j$, $\hat{W}_{j+1/2}$, $\hat{K}_j$ from the predicted step. The final "corrected" value is obtained by averaging the values calculated from the predicted and the corrected steps:

$$\hat{\bar{c}}_j = \bar{c}_j^{(n-1)} + \frac{\Delta t}{2\rho^s} \left[RHSC_j^{(n-1)} + \widehat{RHSC}_j \right] \tag{4.40}$$

$$\hat{U}_j = \frac{U_j^{(n-1)} + \frac{\Delta t}{2} \left[RHSC_j^{(n-1)} + \widehat{RHSU}_j \right]}{1 + \frac{\Delta t}{2} \left[\beta_j^{(n-1)} + \hat{\beta}_j \right]} \tag{4.41}$$

$$\hat{W}_{j+1/2} = \frac{W_{j+1/2}^{(n-1)} + \frac{\Delta t}{2}\left[RHSW_{J+1/2}^{(n-1)} + \widehat{RHSW}_{j+1/2} \right]}{1 + \frac{\Delta t}{2}\left[\beta_{j+1/2}^{(n-1)} + \hat{\beta}_{j+1/2} \right]} \tag{4.42}$$

and

$$\hat{K}_j = \frac{K_j^{(n-1)} + \frac{\Delta t}{2}\left[RHSK_j^{(n-1)} + \widehat{RHSK}_j \right]}{1 + \frac{\Delta t}{2}\left[2\left(\beta_j^{(n-1)} + \hat{\beta}_j \right) + \left(\gamma_{0j}^{(n-1)} + \hat{\gamma}_{0j} \right) \right]} \tag{4.43}$$

The two-step method is employed throughout the computational domain until convergence is satisfied. The convergence criterion is reached when the relative difference between two successive time-steps is less than 0.001.

4.3.2 Fluid Phase Equations

Similar to the sediment phase equations, the fluid phase equations are solved using the two-phase projection method. Incorporating the fluid phase continuity equation in the horizontal and vertical momentum equations, one obtains

$$\begin{aligned} \frac{\partial \widetilde{u}^f}{\partial t} = & -\widetilde{w}^f \frac{\partial \widetilde{u}^f}{\partial z} - \frac{1}{\rho^f}\frac{\partial \overline{P}^f}{\partial x} + \frac{1}{\rho^f\left(1-\overline{c}\right)}\frac{\partial \tau_{xz}^f}{\partial z} \\ & - Sg - \frac{\beta}{\rho^f\left(1-\overline{c}\right)}\left(\overline{c}\widetilde{u}^f - \overline{c}\widetilde{u}^s \right) \end{aligned} \tag{4.44}$$

$$\begin{aligned} \frac{\partial \widetilde{w}^f}{\partial t} = & -\widetilde{w}^f \frac{\partial \widetilde{w}^f}{\partial z} - \frac{1}{\rho^f}\frac{\partial \overline{P}^f}{\partial z} + \frac{1}{\rho^f\left(1-\overline{c}\right)}\frac{\partial \tau_{zz}^f}{\partial z} \\ & - g - \frac{\beta}{\rho^f\left(1-\overline{c}\right)}\left(\overline{c}\widetilde{u}^f - \overline{c}\widetilde{u}^s \right) + \frac{\beta}{\rho^f\left(1-\overline{c}\right)}\upsilon_{ft}\frac{\partial \overline{c}}{\partial z} \end{aligned} \tag{4.45}$$

The horizontal fluid pressure gradient term in equation (4.44) is a known quantity as it represents the driving force for the flow. The horizontal momentum equation is given as

$$\widetilde{u}_j^{f(n)} = \frac{\widetilde{u}_j^{f(n-1)} + \Delta t\left[CFX^{(n-1)} + SFX^{(n-1)} - Sg + \dfrac{\beta^{(n)}}{\rho^f\left(1-\overline{c}^{(n)}\right)}\dfrac{U^{(n)}}{\rho^s}\right]_j}{1+\Delta t\dfrac{\beta_j^{(n)}}{\rho^f\left(1-\overline{c}_j^{(n)}\right)}} \tag{4.46}$$

The vertical fluid velocity is calculated without the vertical pressure gradient as

$$\hat{\widetilde{w}}_{j+1/2}^{f} = \frac{\widetilde{w}_{j+1/2}^{f(n-1)} + \Delta t\left[CFZ^{(n-1)} + SFZ^{(n-1)} + \dfrac{\beta^{(n)}}{\rho^f\left(1-\overline{c}^{(n)}\right)}\left(\dfrac{W^{(n)}}{\rho^s} + \upsilon_{ft}^{n-1} + \dfrac{\partial\overline{c}^{(n)}}{\partial z} + g\right)\right]_{j+1/2}}{1+\Delta t\dfrac{\beta_{j+1/2}^{(n)}}{\rho^f\left(1-\overline{c}_{j+1/2}^{(n)}\right)}} \tag{4.47}$$

The vertical pressure gradient in the momentum equation is unknown and it solved along with the fluid continuity equation and the pressure Poisson equation

$$\frac{\partial}{\partial z}\left[\left(1-\overline{c}^{(n)}\right)\frac{\partial\overline{P}^{f(n)}}{\partial z}\right]_j = \frac{\rho^f}{\Delta t}\left[\frac{\partial\left(1-\overline{c}^{(n)}\right)}{\partial z} - \frac{\partial\left(1-\overline{c}\right)}{\partial t}\right]_j \tag{4.48}$$

The above equation results in a tri-diagonal matrix and is solved using the Thomas algorithm (Hsu, 2002).

The fluid phase convection terms CFX, CFZ and the stress terms SFX, SFZ are calculated similarly as in the sediment phase equations (4.9), (4.17), (4.11) and (4.19).

After the pressure is updated at time-step *n* the vertical fluid velocity is updated at the same time level using

$$\widetilde{w}_{j+1/2}^{f(n)} = \hat{\widetilde{w}}_{j+1/2}^{f} - \frac{1}{\rho^f}\left(\frac{\partial\overline{P}^{f(n)}}{\partial z}\right)_{j+1/2} \tag{4.49}$$

4.4 Stability Analysis

The time-step is dynamically adjusted at every time level based on the numerical stability criterion. From the convective terms of fluid and sediment phase momentum equations, the following Courant condition is obtained

$$\Delta t \le \frac{\eta_1 \Delta z}{\max\left(\left|\tilde{w}^f\right|, \left|\tilde{w}^s\right|\right)} \tag{4.50}$$

Where the numerical coefficient η_1 is taken as 0.3 (Hsu, 2002).

The numerical stability due to the diffusion term in the fluid and sediment equations is defined by

$$\Delta t \le \frac{\Delta z^2}{\max\left[\upsilon_{ft}, \left(\delta AE / \rho^s + \upsilon_{st}\right)\right]} \tag{4.51}$$

Where $\left(\delta AE / \rho^s + \upsilon_{st}\right)$ is the diffusion coefficient in equation (3.45).

The interaction terms in the momentum equation represent the drag force. Constraining the time-step due to the drag force indicates that the size of the time-step is proportional to the particle response time t_p divided by the particle specific gravity s .This is given as

$$\Delta t \le \frac{\eta_2 t_p}{s} \tag{4.52}$$

Where η_2 =0.1 is a numerical coefficient. The minimum of criteria (4.50), (4.51), (4.52) is considered as the minimum size of the time-step.

CHAPTER 5
RESULTS AND ANALYSIS

5.1 Preamble

In this chapter model simulation results for a selected set of conditions at the head of the bed with respect to the initial water level (held constant), particle size current-induced forcing and suspended sediment concentration are presented. Referring to Fig. 5.1 the model is run first in a pre-test mode with a horizontal bottom, which permits the development of the initial conditions with respect boundary layer velocity and suspended sediment concentration. This run is followed by the test run from which as assessment is made of the state of the flow as it develops.

The physical interpretation of model use is shown in Fig. 5.1 on a schematic basis. Fig. 5.1a schematizes the pre-test mode in which a downstream gradient in the pressure force in a horizontal channel leads to the development of the velocity and concentration profiles. During the test run for a sloping channel, sediment suspended is shown to deposit, which means that auto-suspension does not occur in this case. The depth-mean suspended sediment flux $F(x_0)$ (per unit width of channel) at any distance x_0 along the slope is defined as

$$F = \frac{1}{h}\int_0^h u(x_0, z)c(x_0, z)dz \tag{5.1}$$

where c is the concentration in units of kg/m^3. Absence of ignition would mean that the flow is decelerating, i.e. $U_x = dU/dx < 0$, where U is the depth-mean current velocity. Also the flux gradient $F_x = dF/dx$ must be negative. The opposite conditions prevail when the conditions are conducive to ignition (Fig. 5.1b). Thus in the present study ignition or the ignitive condition is defined as one in which $dU/dx > 0$ and $dF/dx > 0$ and auto-suspension is defined as the stage if the Shields parameter is above the Bagnold auto-suspension curve as shown in Figure 5.10. It should be pointed out that a condition can also exist when these two criteria are satisfied and yet

dc/dx is negative, i.e. a depositing turbidity current occurs even when the flow is accelerating so rapidly that dF/dx is also positive. However, such a condition cannot last indefinitely, because the accelerating current will eventually erode the bed at such a rate that the gradient dc/dx will become greater than zero.

In the present analysis the pre-test water depth is kept constant (at 0.12 m) and conditions for ignition are examined by varying the particle size d, the pressure gradient and the bed slope α. For particle size, three medium-sized beach sands typically found in Florida (Dean and Dalrymple, 2002) are selected; these being 0.21 mm, 0.28 mm and 0.35 mm. The pressure gradient is specified in terms of the friction velocity u_* per Eq. 3.63. Since the channel is assumed to be hydraulically wide, the hydraulic radius (r_b) is replaced by water depth h. The bed slope is varied between 0° and 17°; however, results for slopes lower than 12° indicated that no ignition could occur for the selected ranges of diameters and friction velocities.

The choice of three values each of d, u_* and α lead to 54 pre-test runs and corresponding test runs. The selected combinations of these three variables are given in Tables 5.1, 5.2 and 5.3.

The outcome of the pre-test mode of model simulation supplies the initial velocity profile and the concentration profile for the turbidity current on the slope. As an illustration, model output in terms of the development of the velocity field and concentration field for d = 0.21 mm, u_* = 0.06 m/s and $\alpha = 0^o$ is shown in Fig. 5.2. Note that time is represented along the abscissa as the model is 1DV. The time profile of the velocities taken at different heights is plotted. It is observed that in the absence of any driving force after 150 s, the flow dies down. Another perspective of the same occurrence can be observed in Figure 5.2b in which the velocity profile is plotted at different times. It is noticed that from the initial point at 150 s where the pressure forcing is stopped and the gravitational components are required to take over, in the absence of

any slope, the velocity decreases. In Fig. 5.2c, in which the volumetric concentration profile is plotted, it is discernible that there is no suspension; in fact the bed suspension simply dies down. It is also noticed from Fig. 5.2b that the velocity profile does not quite begin from the origin but at an ordinate above the origin. This region includes the solid bed below in which the flow was not able to suspend any sediment and also the bed over which these is a flow. This feature can also be noticed in Fig. 5.3 and 5.4 where the results from Parker et al. (1987) are compared against the model.

5.2 Experimental Data and Model Output

Ignitive turbidity currents have been predicted by numerical models (e.g. Eidsvik and Brøs, 1989); however it appears that laboratory test results have been unable to fully verify modeling outcomes. As we noted in Chapter 3, the laboratory tests of Parker et al. (1987) showed ignition in two tests out of the 24 they conducted. Their data on the evolution of velocity and concentration profiles offer the possibility of testing the performance of the present numerical model. However, since the model has been configured by the original developer (Hsu, 2002) for specific types of two-phase flow conditions (limited to sand grains and very high-density packing), and because its reconfiguration was beyond the present scope, it was decided to use the model for a qualitative comparison with one dataset of Parker et al.

Figures 5.3 to 5.5 show measured profiles (dashed lines) of velocity and concentration at three distances from the upstream end of the laboratory channel (shown in Fig. 2.5) in a single run. Solid-line curves indicate the velocity and concentration profiles obtained from the model run. The input data used for this run were the closest possible that could be used to simulate conditions in Parker et al. test. The modeled diameter of sediment grain was 0.20mm, compared to 0.03mm in the experiment. The initial layer-averaged velocity U_0 in the model run was 0.13 m/s compared to 0.27m/s in the experiment. This velocity of 0.13 m/s was used to convert time-

dependent profiles from the model output to distance dependent profiles plotted in the figures. The bed slope was 3° in both cases. Finally, the initial volume concentration C_v of the bottom material in the experiment was 0.0041, whereas the model was based on C_v = 0.635, a significantly high value.

The velocity and concentration profiles at a distance of x = 1.5m in Figs. 5.3, 5.4 and 5.5 show expected quantitative differences but at the same time demonstrate that the model results are reasonable. From these plots the quantities $\dot{F} = dF/dt, F_x$ and U_x are calculated and given in Table 5.4. The differences between the experimental evidence and the model output are due to differences in the sediment size. In the experiments fine-grained (but non-cohesive) sediment was used. This is coupled with the fact that when compared to the model, the very low volumetric concentration in the experimental run led to an accelerating flow which was sensitive to the initial conditions specified by an initial velocity of 0.27 m/s and a sediment discharge of 0.165 kg/s. Parker et al. mention that in most runs they could observe an accelerating yet depositing current. As mentioned, one of the reasons they cite is that the short length of the flume in which the experiments were carried out possibly did not allow them to witness ignition. In the model larger sediment was used with large concentration and a low angle of inclination which led to the damping of the flux. Also, as noted the concentration was very low in the experiments in comparison with the model, in which the stationary bed had random close packing concentration.

5.3 Domain of Ignitive Behavior

Results of model test runs corresponding to the conditions set in Tables 5.1, 5.2 and 5.3 are given in Tables 5.5, 5.6 and 5.7, respectively. These results are conveniently plotted in terms of the Shields parameter (along the ordinate)

$$\theta = \frac{u_*^2}{(s-1)gd} \tag{5.2}$$

Where s, the specific weight of the particles, is taken as 2.65 in the present study (e.g. Julien, 1995).

In Fig. 5.6, θ is plotted against bed slope and includes the results from the model test runs. As mentioned earlier, in the 24 tests they performed, only two were in the regime of accelerating flow and eroding sediment. However, as also mentioned previously they could not observe any catastrophic development. The points that correspond to ignition are denoted by the symbol "*I*" and those that correspond to a non-ignitive state are denoted by "*N*".

As an extension of Fig. 5.6, contours of sediment flux per unit width F (kg/m^3/s) for each grain size are plotted in Figs. 5.7, 5.8 and 5.9. It is difficult to identify the presence of an accelerating eroding current based on the intensity of the sediment flux, as erosion occurs albeit at a small rate in comparison to the next condition of an increased angle where the flux is many times higher. However, it can be said with certainty that self-sustaining capability is encouraged with increasing slope. It is also uncertain why, for the smallest diameter of 0.21mm in Fig. 5.7 the flux has its highest value at a slope of 16° but then decreases as the slope is increased. Such a trend is not observed in Figs. 5.8 or 5.9 for the larger diameters.

The mass fluxes in Tables 5.5 to 5.7 were calculated at distance x = 20 m from the beginning of the slope. Either erosion or deposition is noticeable at this distance. To calculate the Shields parameter at this point, the depth mean velocity was evaluated and the friction velocity was calculated from

$$u_* = \sqrt{C_d}U \tag{5.3}$$

The drag coefficient was calibrated to the value 0.018 by taking into account Fig. 5.10 such that the value of C_d did not cause the Shields parameter calculated from the friction velocity obtained from Eq. 5.3 to fall below the threshold of the incipient motion.

It is observed from Fig. 5.7 that the flux obtained does not increase with increase in the slope above 16°. Comparison with Fig. 5.10 can be shown to indicate that the maximum Shields parameter is not obtained at larger slopes but rather at the condition where the initial forcing friction velocity at the start was a maximum. In Fig. 5.7 the maximum flux seems to be associated with the flow conditions and not uniquely to the slope.

The plot in Fig. 5.8 seems to suggest a "transitory" regime where the combined influence of the slope and the initial condition is witnessed. It is observed that the flux increases with increase in slope but not as consistently as in Fig. 5.9 where it is clearly observed that the flux increases with the slope.

In Fig. 5.10 the Shields parameter is plotted as a function of the grain size along with Shields threshold curve for incipient grain movement and the Bagnold auto-suspension curve. Data points from the model test runs are superimposed. It is observed that all the data points denoted by 'I' (ignitive) and 'N' (non-ignitive) in Fig. 5.6 represent auto-suspensions. This trend is observed sediment of diameter 0.21mm and 0.28mm.Whereas for sediment diameter 0.35mm three of the cases are between bedload and auto-suspension. These three cases are for the slopes of 12°, 13° and 14° and the initial forcing condition in each of them is $u_* = 0.06$ m/s (at the onset of the pre-test run). This is in contradiction to the condition of self-acceleration where both dU/dx and dF/dx are greater than zero as it includes all the data sets which were mentioned as non-ignitive in nature.

Table 5.1 Model runs for grain size of 0.21mm

Run no.	Particle diameter, d (mm)	Initial friction velocity, u_* (m/s)	Bed slope, α (degrees)
1	0.21	0.06	12
2	0.21	0.07	12
3	0.21	0.08	12
4	0.21	0.06	13
5	0.21	0.07	13
6	0.21	0.08	13
7	0.21	0.06	14
8	0.21	0.07	14
9	0.21	0.08	14
10	0.21	0.06	15
11	0.21	0.07	15
12	0.21	0.08	15
13	0.21	0.06	16
14	0.21	0.07	16
15	0.21	0.08	16
16	0.21	0.06	17
17	0.21	0.07	17
18	0.21	0.08	17

Table 5.2 Model runs for grain size of 0.28mm

Run no.	Particle diameter, d (mm)	Initial friction velocity, u_* (m/s)	Bed slope, α (degrees)
19	0.28	0.06	12
20	0.28	0.07	12
21	0.28	0.08	12
22	0.28	0.06	13
23	0.28	0.07	13
24	0.28	0.08	13
25	0.28	0.06	14
26	0.28	0.07	14
27	0.28	0.08	14
28	0.28	0.06	15
29	0.28	0.07	15
30	0.28	0.08	15
31	0.28	0.06	16
32	0.28	0.07	16
33	0.28	0.08	16
34	0.28	0.06	17
35	0.28	0.07	17
36	0.28	0.08	17

Table 5.3 Model runs for grain size of 0.35mm

Run no.	Particle diameter, d (mm)	Initial friction velocity, u_* (m/s)	Bed slope, α (degrees)
37	0.35	0.06	12
38	0.35	0.07	12
39	0.35	0.08	12
40	0.35	0.06	13
41	0.35	0.07	13
42	0.35	0.08	13
43	0.35	0.06	14
44	0.35	0.07	14
45	0.35	0.08	14
46	0.35	0.06	15
47	0.35	0.07	15
48	0.35	0.08	15
49	0.35	0.06	16
50	0.35	0.07	16
51	0.35	0.08	16
52	0.35	0.06	17
53	0.35	0.07	17
54	0.35	0.08	17

Table 5.4 Flow state in experiment and model run

Reach (m)	$\dot{F}$ (kg/m^3/s^2)		F_x (kg/m^4/s)		U_x (1/s)		Flow state	
	Data	Model	Data	Model	Data	Model	Data	Model
1.5-4.5	8.5×10^{-5}	-6.5×10^{-4}	-3.1×10^{-3}	-7.7×10^{-3}	1.0×10^{-3}	-1.9×10^{-2}	Acc./ dep	Dec./dep
4.5-8.5	-5.3×10^{-3}	-7.3×10^{-5}	-7.4×10^{-3}	-8.6×10^{-4}	6.0×10^{-4}	-5.7×10^{-3}	Acc./ dep	Dec./dep

Table 5.5 Flow states for 0.21mm particles

Run no.	$\dot{F}$ (kg/m^3/s^2)	F_x (kg/m^4/s)	U_x (1/s)	Flow state
1	-0.009	-0.021	-0.009	Decel./depos.
2	-0.020	-0.028	-0.008	Decel./depos.
3	-0.034	-0.030	-0.006	Decel./depos.
4	-0.008	-0.016	-0.007	Decel./depos.
5	-0.018	-0.024	-0.006	Decel./depos.
6	-0.032	-0.026	-0.005	Decel./depos.
7	-0.010	-0.018	-0.007	Decel./depos.
8	-0.020	-0.025	-0.005	Decel./depos.
9	-0.024	-0.019	-0.003	Decel./depos.
10	-0.008	-0.014	-0.005	Decel./depos.
11	-0.015	-0.018	-0.004	Decel./depos.
12	-0.025	-0.018	-0.002	Decel./depos.
13	-0.009	-0.015	-0.004	Decel./depos.
14	1.804	0.524	0.015	Accel./eros.
15	0.005	0.003	0.0004	Accel./eros.
16	0.017	0.020	0.002	Accel./eros.
17	0.014	0.012	0.001	Accel./eros.
18	0.062	0.030	0.005	Accel./eros.

Table 5.6 Flow states for 0.28mm particles

Run no.	$\dot{F}$ ($kg/m^3/s^2$)	F_x ($kg/m^4/s$)	U_x (1/s)	Flow state
19	-0.008	-0.026	-0.013	Decel./depos.
20	-0.015	-0.033	-0.011	Decel./depos.
21	-0.026	-0.037	-0.008	Decel./depos.
22	-0.008	-0.026	-0.011	Decel./depos.
23	-0.016	-0.031	-0.008	Decel./depos.
24	-0.022	-0.029	-0.006	Decel./depos.
25	-0.009	-0.026	-0.009	Decel./depos.
26	-0.016	-0.028	-0.006	Decel./depos.
27	-0.015	-0.017	-0.004	Decel./depos.
28	-0.010	-0.025	-0.006	Decel./depos.
29	-0.015	-0.022	-0.003	Decel./depos.
30	0.668	0.460	0.010	Accel./eros.
31	1.042	0.397	0.015	Accel./eros.
32	1.330	0.392	0.014	Accel./eros.
33	0.009	0.008	0.002	Accel./eros.
34	1.073	0.370	0.012	Accel./eros.
35	1.025	0.333	0.011	Accel./eros.
36	1.190	0.327	0.010	Accel./eros.

Table 5.7 Flow states for 0.35mm particles

Run no.	$\dot{F}$ ($kg/m^3/s^2$)	F_x ($kg/m^4/s$)	U_x (1/s)	Flow state
37	-0.007	-0.034	-0.016	Decel./depos.
38	-0.014	-0.041	-0.014	Decel./depos.
39	-0.023	-0.044	-0.011	Decel./depos.
40	-0.009	-0.037	-0.014	Decel./depos.
41	-0.014	-0.037	-0.011	Decel./depos.
42	-0.021	-0.035	-0.007	Decel./depos.
43	-0.009	-0.036	-0.011	Decel./depos.
44	-0.014	-0.031	-0.007	Decel./depos.
45	-0.014	-0.020	-0.003	Decel./depos.
46	-0.007	-0.022	-0.005	Decel./depos.
47	2.063	0.574	0.018	Accel./eros.
48	1.725	0.480	0.015	Accel./eros.
49	2.524	0.484	0.018	Accel./eros.
50	2.401	0.445	0.017	Accel./eros.
51	2.226	0.397	0.015	Accel./eros.
52	2.364	0.397	0.016	Accel./eros.
53	2.266	0.376	0.015	Accel./eros.
54	2.164	0.357	0.015	Accel./eros.

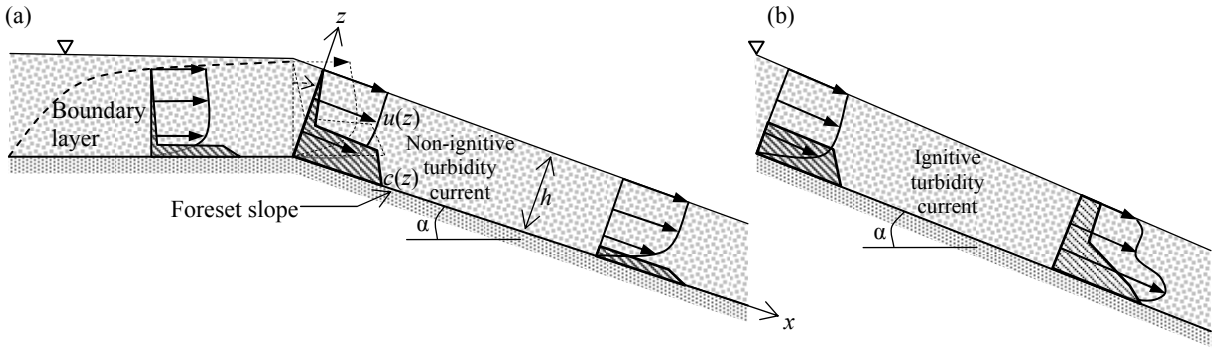

Figure 5.1 Physical interpretation of mode simulations: (a) downstream gradient in pressure force leads to the development of a boundary layer velocity profile and associated profile in the suspended sediment concentration. Under non-ignitive conditions the concentration decreases due to sediment deposition; (b) conditions are conducive for ignition.

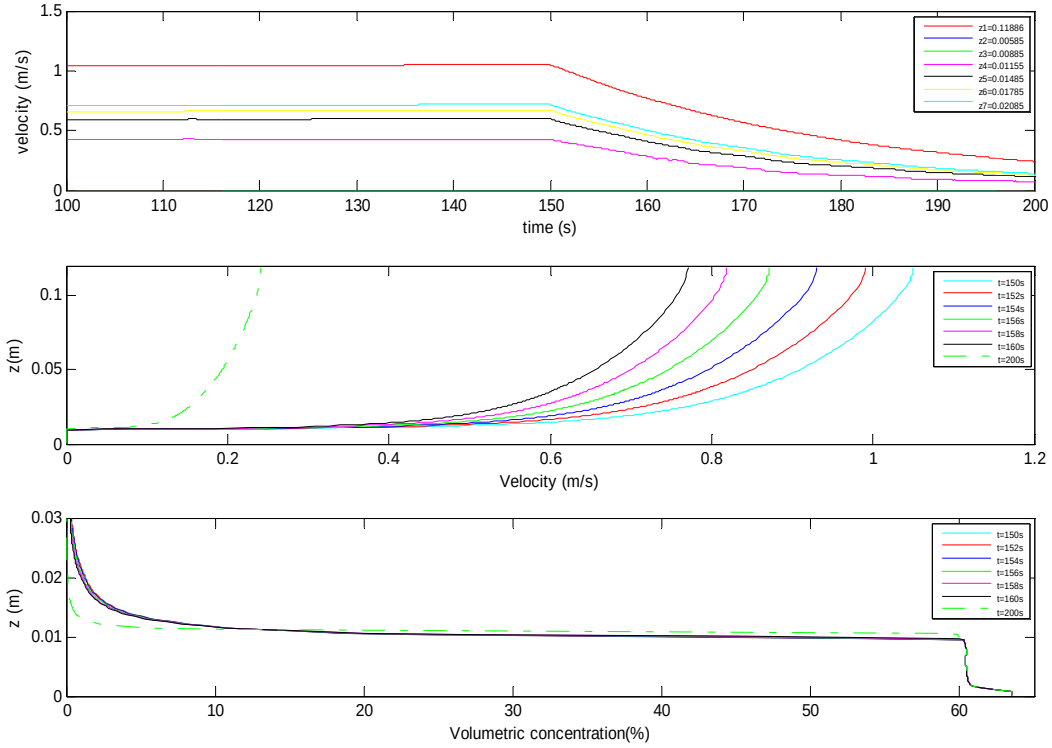

Figure 5.2 Growth of boundary layer velocity and concentration profiles during a pre-test run with d = 0.21mm, u_* = 0.06 m/s and α = 0°.

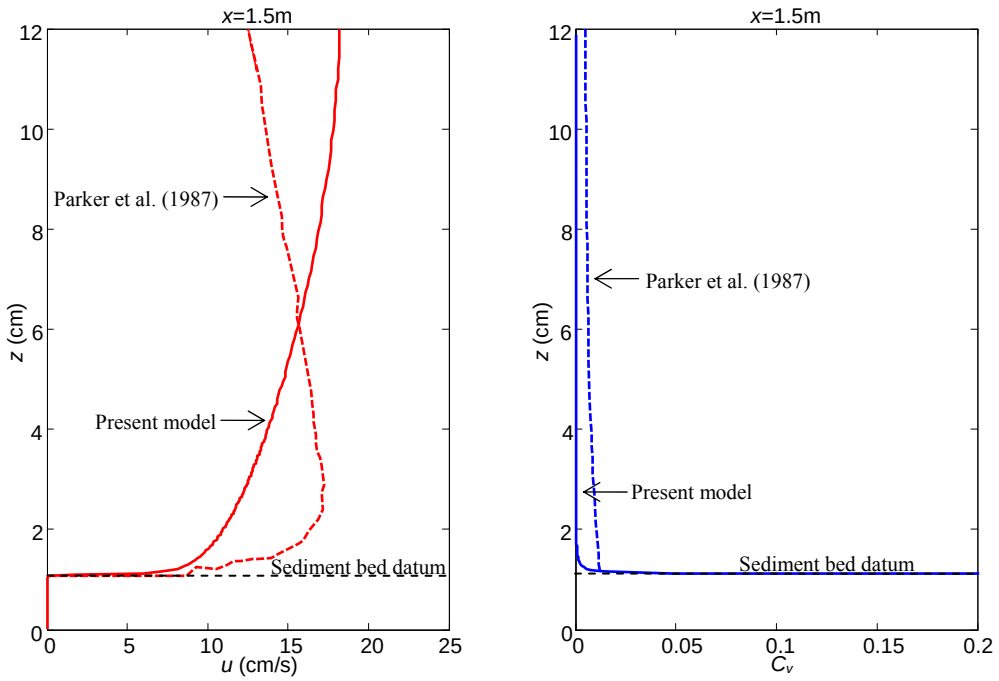

Figure 5.3 Velocity and concentration profiles: Experimental data of Parker et al. (1987) and present model run. The main difference is in the grain size (0.03mm in experiment versus 0.20mm in the model). Both are at a distance of x=1.5m.

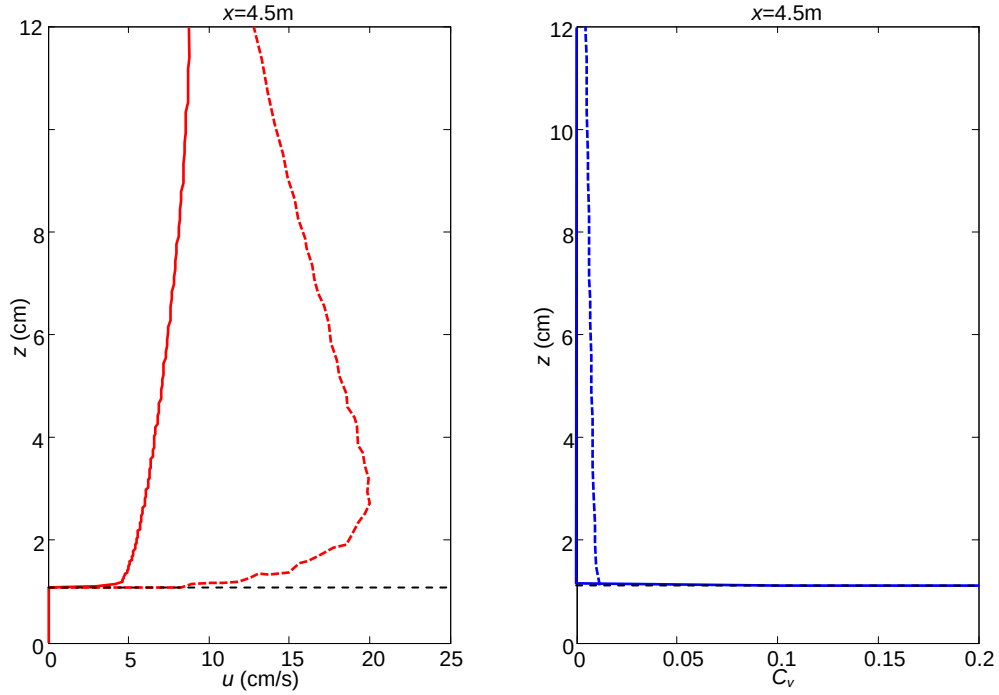

Figure 5.4 Velocity and concentration profiles: Experimental data of Parker et al. (1987) and present model run. The main difference is in the grain size (0.03mm in experiment versus 0.20mm in the model). Both are at a distance of x=4.5m.

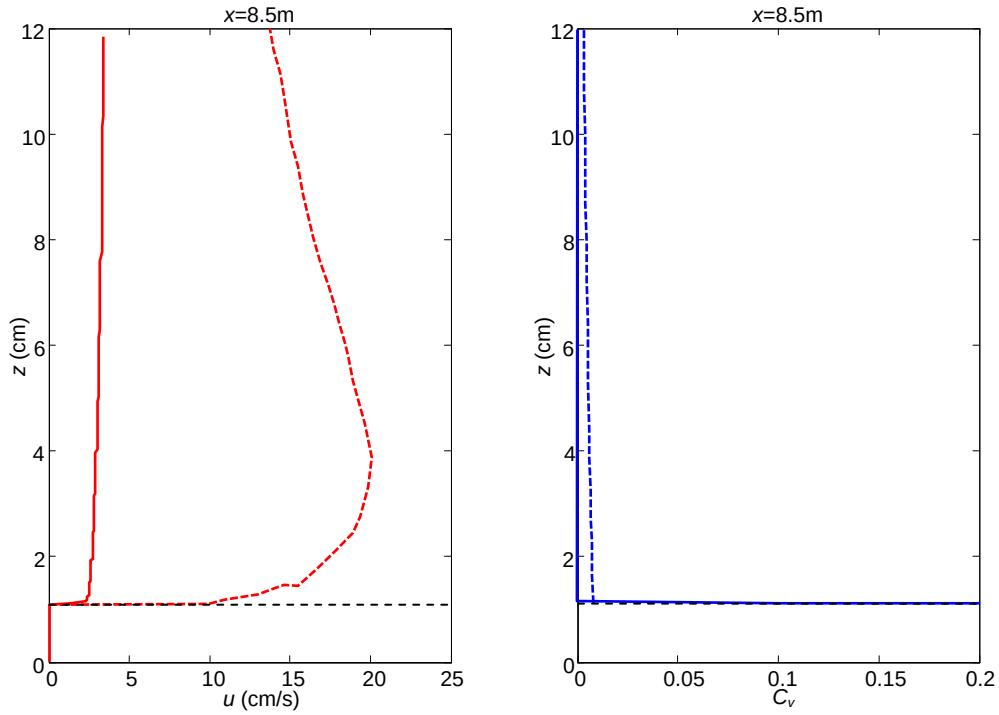

Figure 5.5 Velocity and concentration profiles: Experimental data of Parker et al. (1987) and present model run. The main difference is in the grain size (0.03mm in experiment versus 0.20mm in the model). Both are at a distance of x=8.5m.

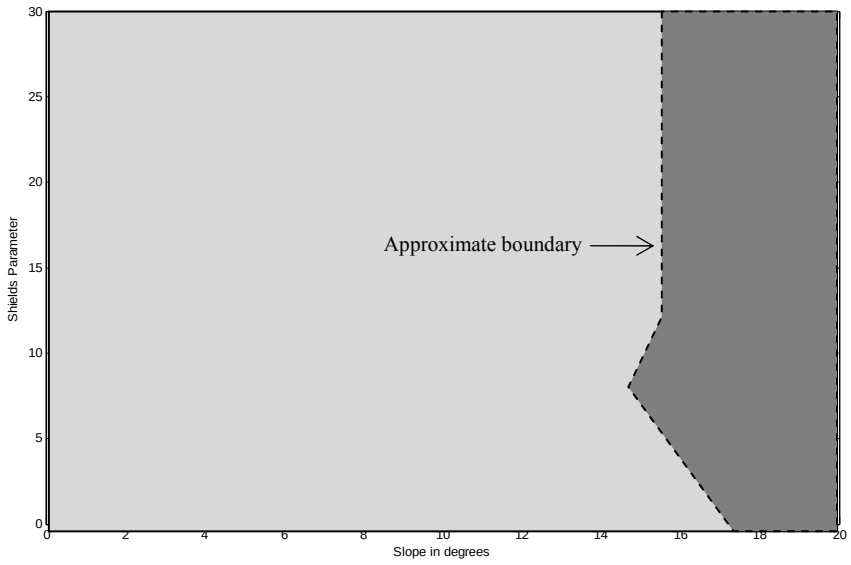

Figure 5.6 Shields parameter against bed slope.

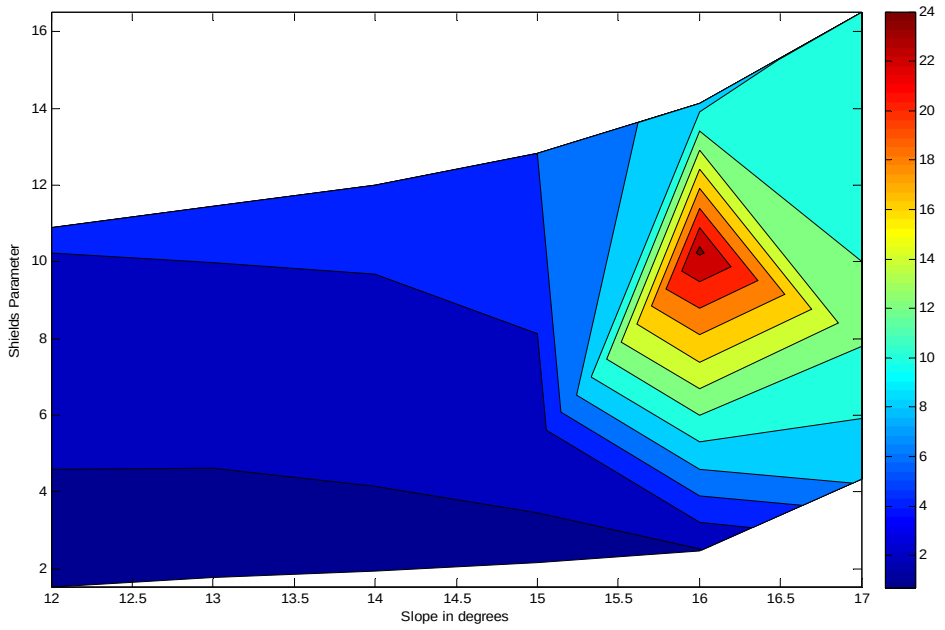

Figure 5.7 Shields parameter against bed slope. Sediment flux per unit width ($kg/m^3/s$) contours for 0.21mm diameter particles.

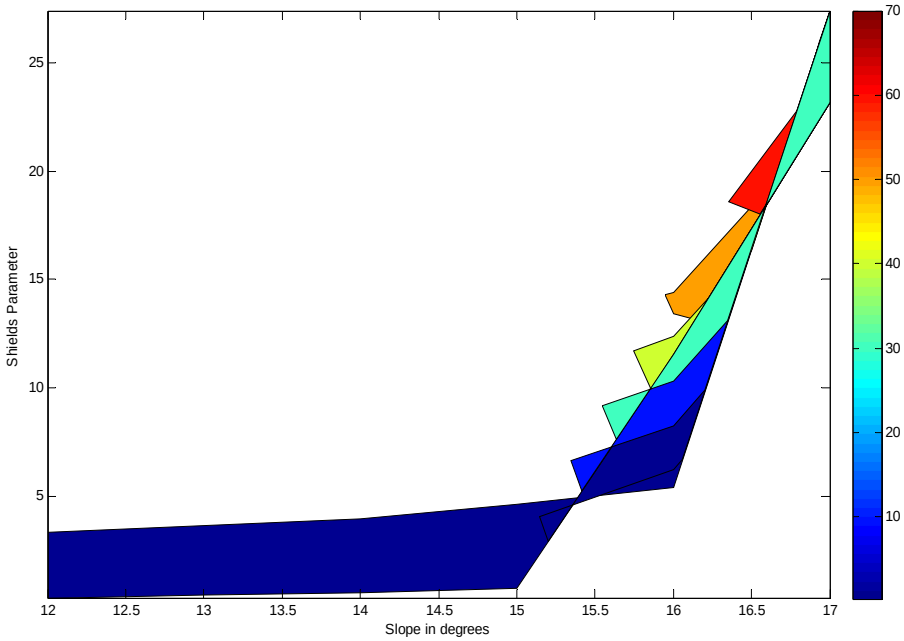

Figure 5.8 Shields parameter against bed slope. Sediment flux per unit width ($kg/m^3/s$) contours for 0.28mm diameter particles.

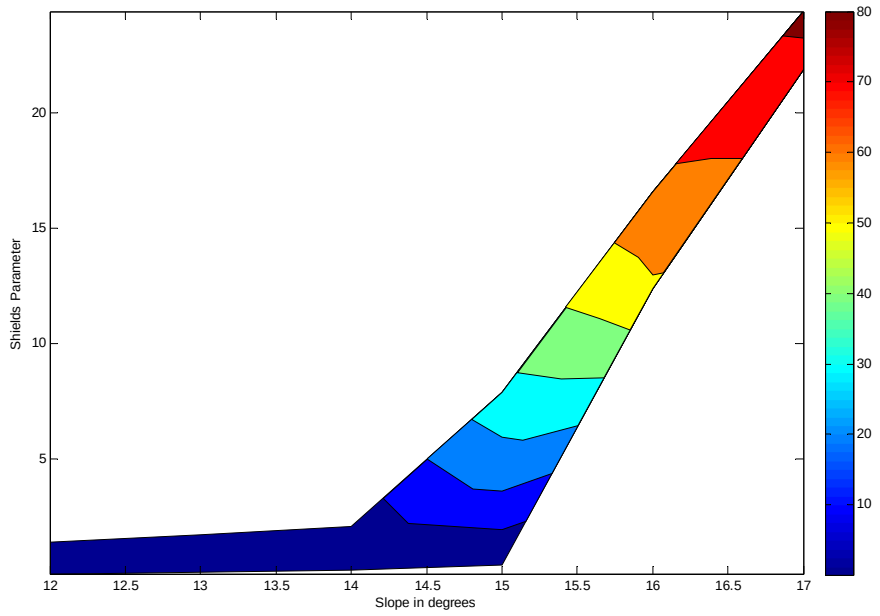

Figure 5.9 Shields parameter against bed slope. Sediment flux per unit width (kg/m^3/s) contours for 0.35mm diameter particles.

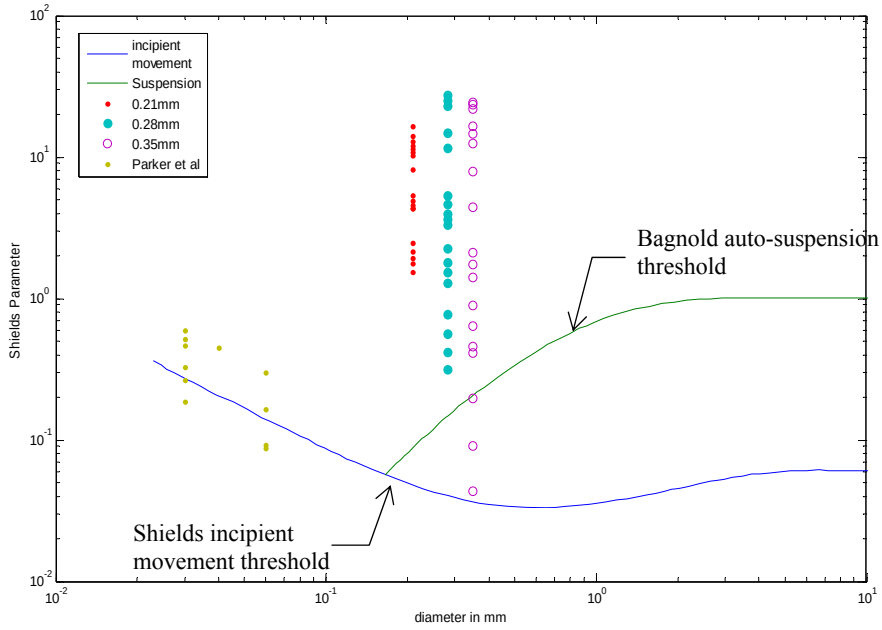

Figure 5.10 Shields parameter against particle diameter. Threshold curves for incipient movement and auto-suspension curve. Model test run data.

CHAPTER 6
SUMMARY, CONCLUSIONS AND RECOMMENDATIONS

6.1 Summary

Turbidity currents form a major mechanism for the transport of sediment from the continental shelf into deeper waters. Self-accelerating turbidity currents is a topic of considerable scientific and engineering interest, because such currents can be self-sustaining and if so be responsible for significant transport of sediment derived ultimately from terrestrial sources to the seabed. Self-acceleration can occur if the flow velocity and the suspended sediment concentration increase simultaneously and entrain additional sediment due to the impelling down-slope gravity force and associated turbulence.

"Ignition" in the present study refers to the onset of self-acceleration of an erosive turbidity current without reference to its subsequent fate. Such a fate could involve excessive densification of the current as erosion continues, collapse of turbulence, and possible destruction of the system as a stream. A condition meant to determine if a current is able to erode bottom sediment and form a suspension (as opposed to bedload) is the Knapp-Bagnold criterion for "auto-suspension". This is a necessary but not a sufficient criterion to ascertain if the turbid current formed will be ignitive or depositional, because an auto-suspension may not satisfy the conditions for self-acceleration. A self-accelerating turbid current has also been called a self-sustaining current.

Most modeling efforts made to date to determine the conditions for ignition are based on the use of single-phase fluids treated as a suspension. In the present analysis an available (Hsu , 2002) one-dimensional (vertical) model, which treats the fluid and particles as separate phases, is used. Experimental data of Parker et al. (1987) have been included as part of the analysis.

The model investigates the effects of particle size, initial flow friction velocity and bed slope on the relationship between the Shields entrainment parameter and the grain size in the

context of the Knapp-Bagnold curve for auto-suspension. Particle sizes are limited to medium sands typical of beaches in Florida. The bed slope is assumes to be small. Because the model is 1DV, flow velocities and suspended sediment concentration are dependent on the vertical coordinate and time but are independent of the horizontal coordinates. Accordingly, the model is used in two phases. At first, by applying a horizontal pressure gradient using lateral ghost grids, a boundary layer velocity profile is allowed to develop in the time domain but considered to be in the (pseudo) horizontal direction. After the boundary layer velocity profile has developed close to a time-independent structure the velocity profile is noted. In the second phase the bottom is tilted, which permits water to flow downslope starting with the velocity at the end of the first phase. The bed in this case contains densely packed but erodible sandy sediment. The evolutions of the velocity and the concentration profiles are tracked in time. By using the depth-mean initial velocity at the head of the slope, time is converted into an approximate distance of travel down the slope. At two selected times (or equivalent distances), the depth-mean velocity and the suspended sediment flux (per unit flow width) are calculated. These are used to calculate the corresponding flow acceleration and flux gradient, which are then used along with the plot of Shields parameter against size to make an assessment of the relationship between the Knapp-Bagnold auto-suspension curve and the ignitive condition.

6.2 Conclusions

The following are the main conclusions reached in this study:

1. Although the two-phase flow model of Hsu (2002) could only be run for a limited range of grain sizes (medium sands similar to those found in Florida beaches) and sediment bed density, comparison with flume experimental data of Parker et al. (1987) indicated that the model produced reasonable results for the velocity and concentration profiles in gravity-driven turbidity currents.

2. Self-acceleration of turbidity current over a bed of sand with the smallest of the three selected sizes (0.21mm) was found to depend on the initial conditions at the head of the slope determined by the imposed pressure gradient in terms of the bed friction velocity. Bed slope seemed to be of secondary importance.
3. For the two sands with larger grain sizes (0.28mm and 0.35mm) the bed slope was found to play a more important role when compared to the initial pressure gradient. For a given pressure gradient, increasing the slope increased the likelihood of self-acceleration.
4. Based on conclusions 2 and 3 it could be concluded that ignition cannot be defined merely in terms of non-trivial, positive values of the velocity gradient and the sediment flux gradient along the slope. Depending on particle size the initial pressure gradient can also play a role.
5. For the selected initial conditions (grain size, pressure gradient and bed slope), out of the 54 combinations tested, all except three satisfied the Knapp-Bagnold criterion for auto-suspension irrespective of whether the turbidity current was ignitive or non-ignitive.
6. In all 54 cases the current was found to be erosive.

6.3 Recommendations for Further Work

1. Bearing the mind that the two-phase flow model has no restrictions relative to, or imposition of, the sediment pick up function or the need for the use of sediment bedload and suspended load equations, the model's evident versatility should be demonstrated by reconfiguring it to accommodate a larger range of the sediment sizes. Model results should be carefully tested against experimental data.
2. The model was used to simulate a physical situation in which boundary layer flows were generated on a horizontal bed for a certain time and then through numerical manipulation subsequent turbidity currents on inclined beds were simulated. It should be possible to switch the inclined surface after a prescribed time back to a horizontal surface. It should then be possible to witness energy loss through a hydraulic jump, or eventual settling of the suspended sediment. Such a numerical experimentation should be verified against experimental data.

APPENDIX A
Numerical Implementation Scheme

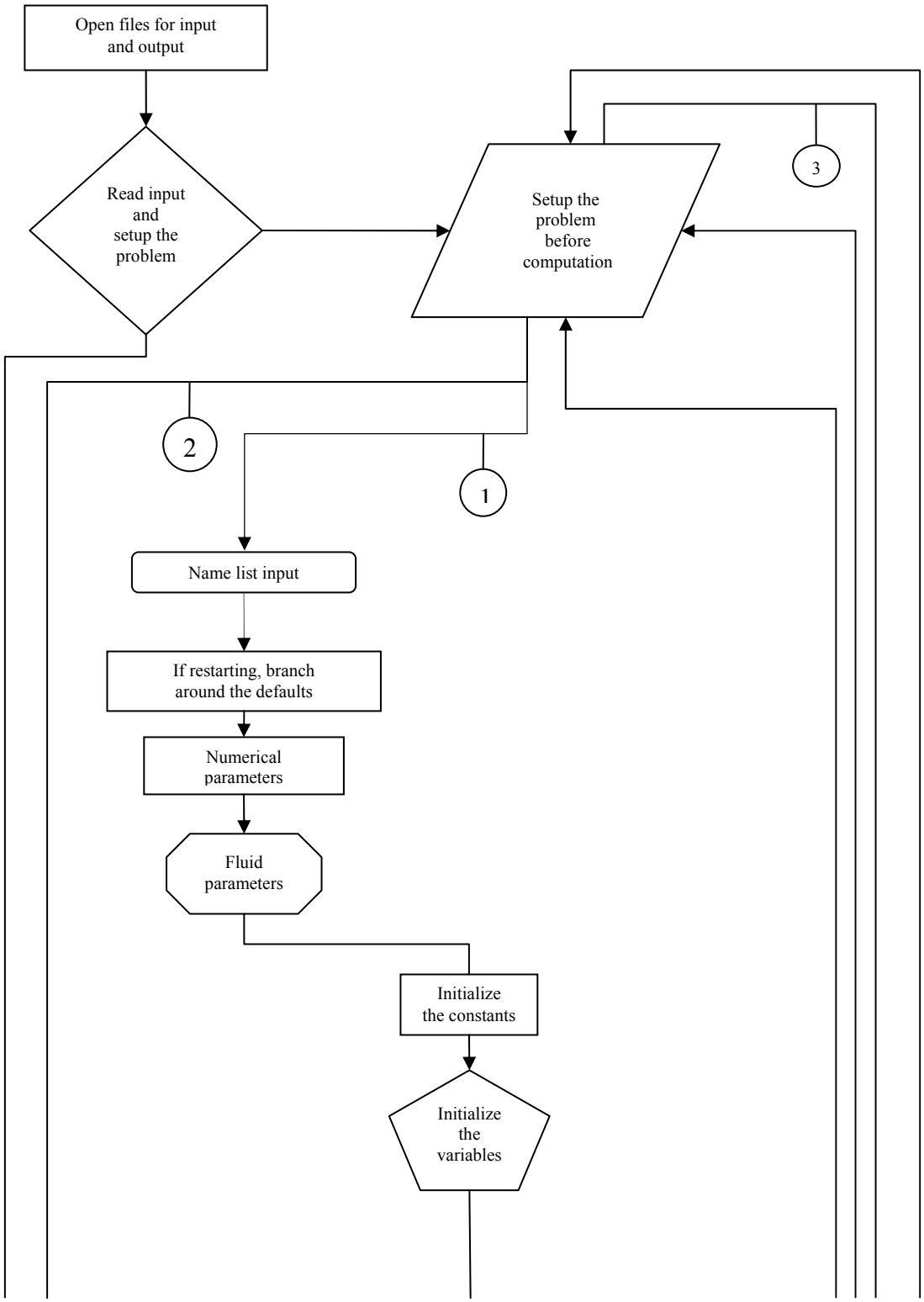

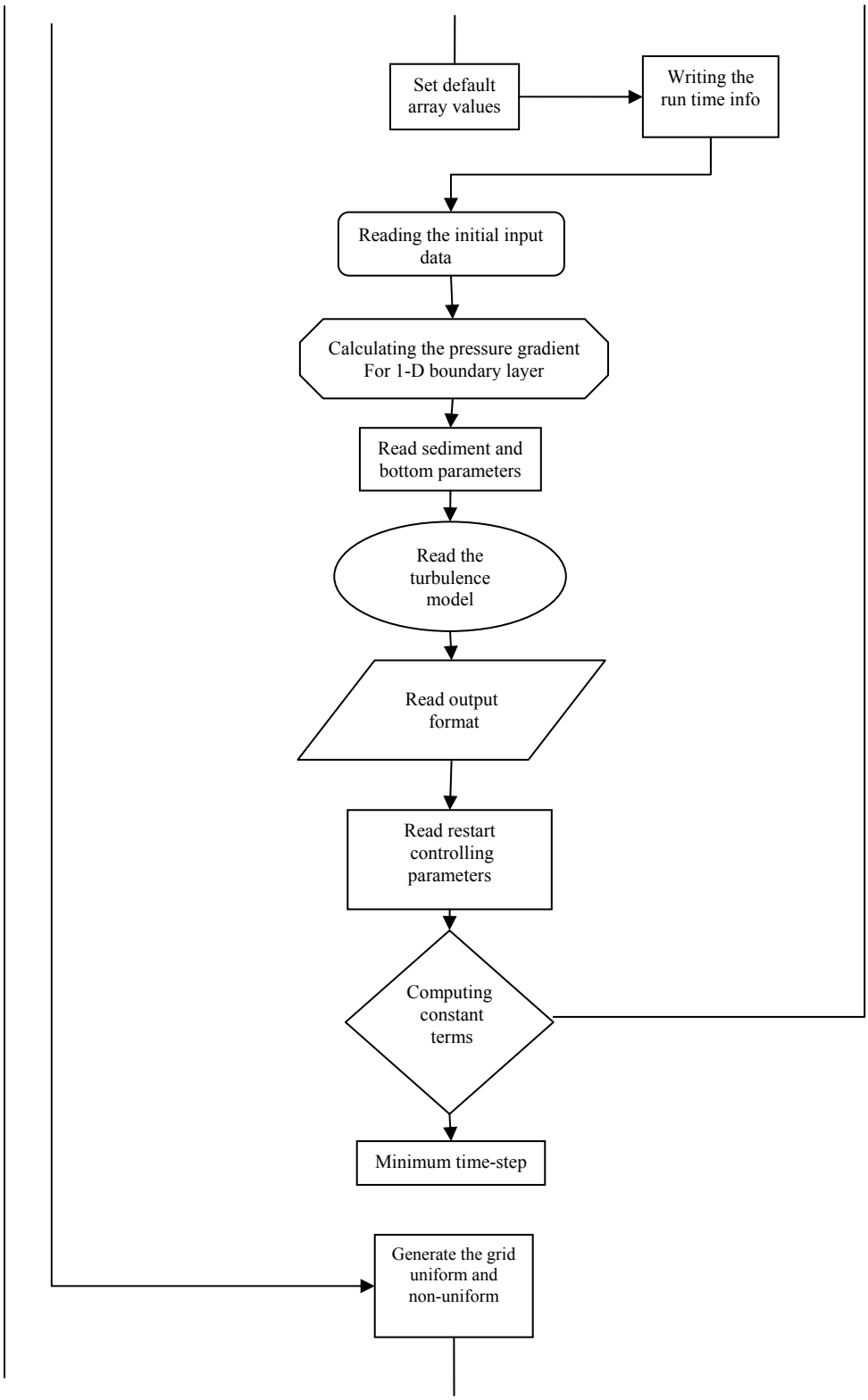
Set default array values
Writing the run time info
Reading the initial input data
Calculating the pressure gradient For 1-D boundary layer
Read sediment and bottom parameters
Read the turbulence model
Read output format
Read restart controlling parameters
Computing constant terms
Minimum time-step
Generate the grid uniform and non-uniform

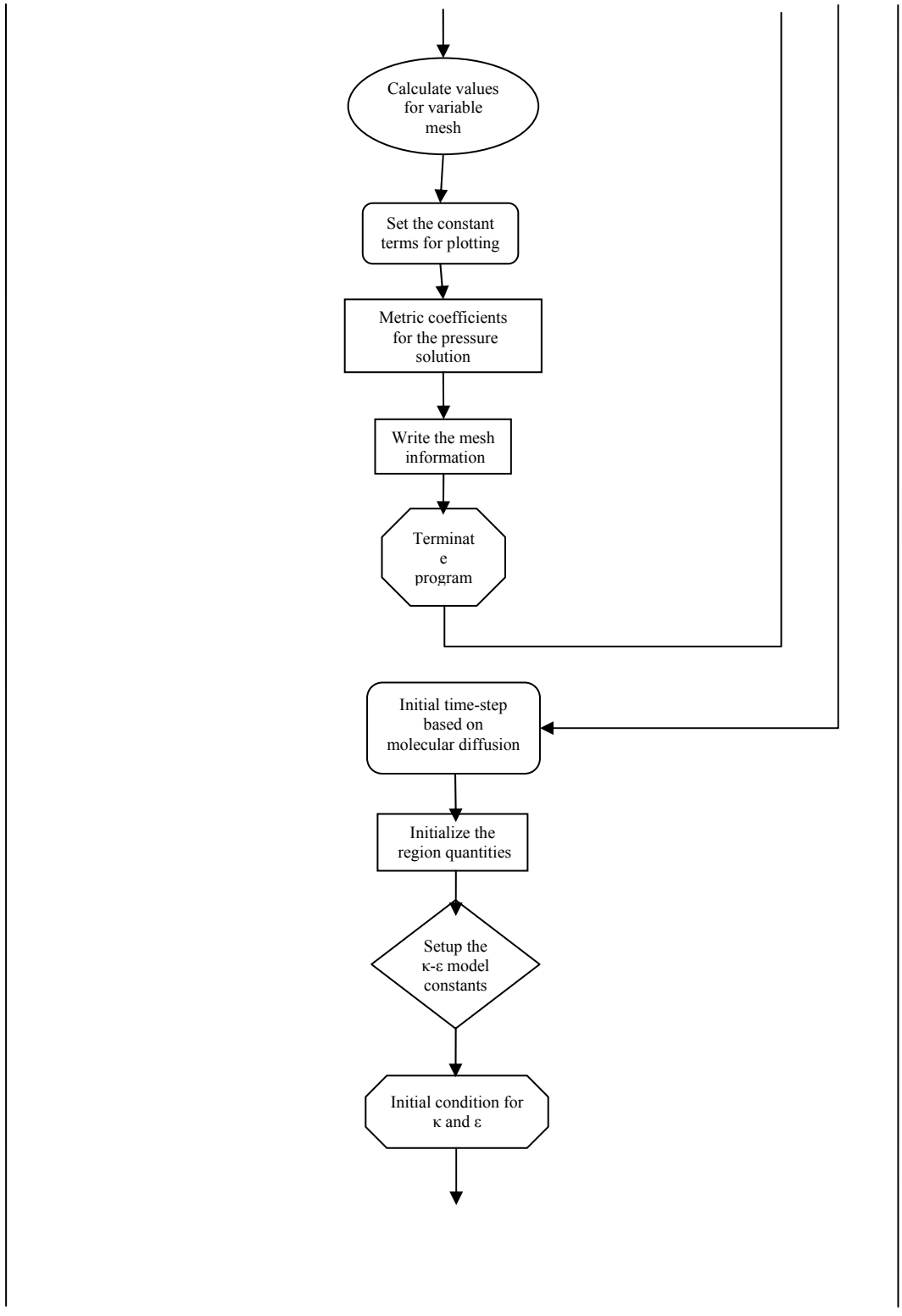
Calculate values for variable mesh
Set the constant terms for plotting
Metric coefficients for the pressure solution
Write the mesh information
Terminat e program
Initial time-step based on molecular diffusion
Initialize the region quantities
Setup the κ-ε model constants
Initial condition for κ and ε

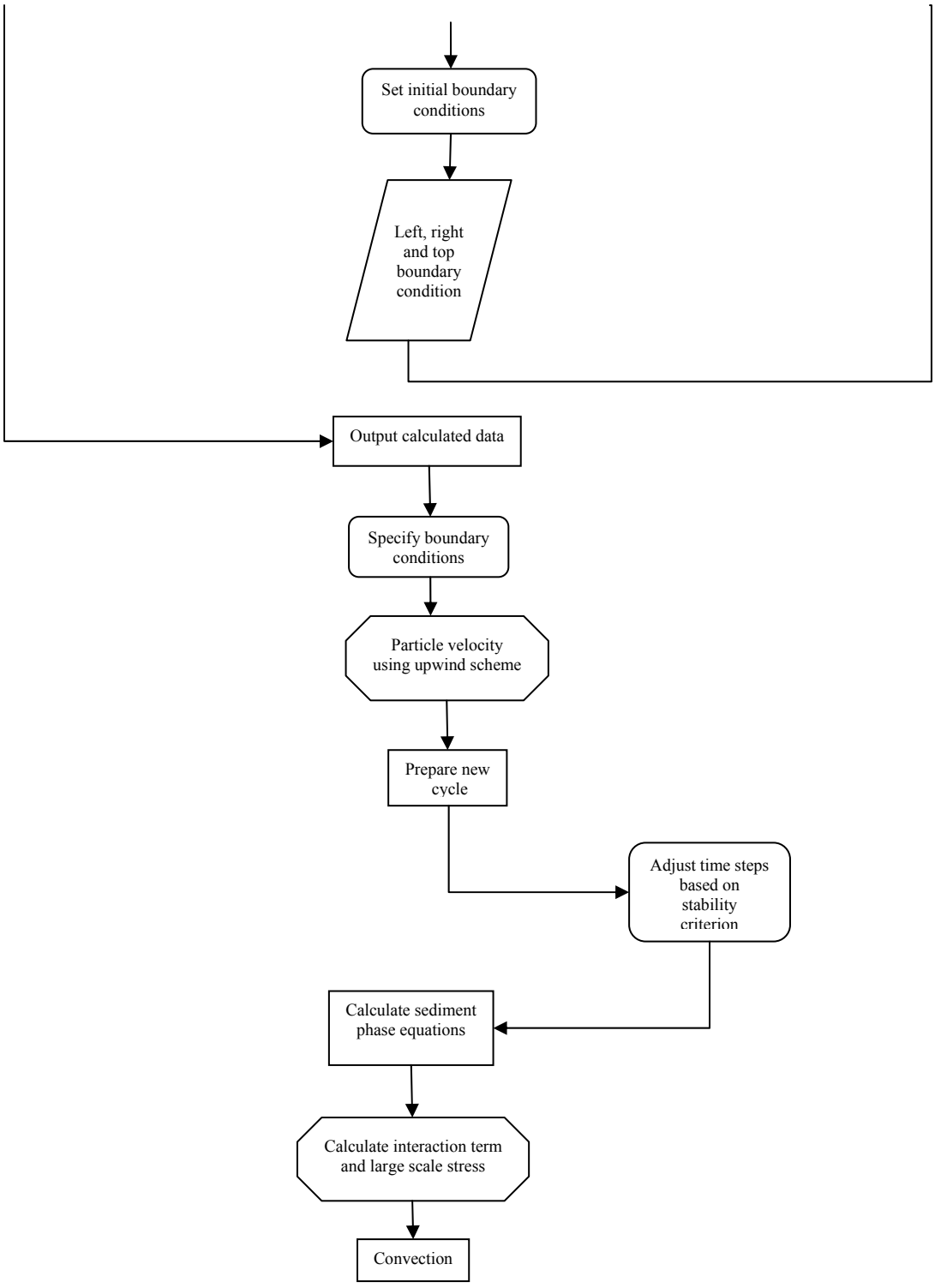
Set initial boundary conditions
Left, right and top boundary condition
Output calculated data
Specify boundary conditions
Particle velocity using upwind scheme
Prepare new cycle
Adjust time steps based on stability criterion
Calculate sediment phase equations
Calculate interaction term and large scale stress
Convection

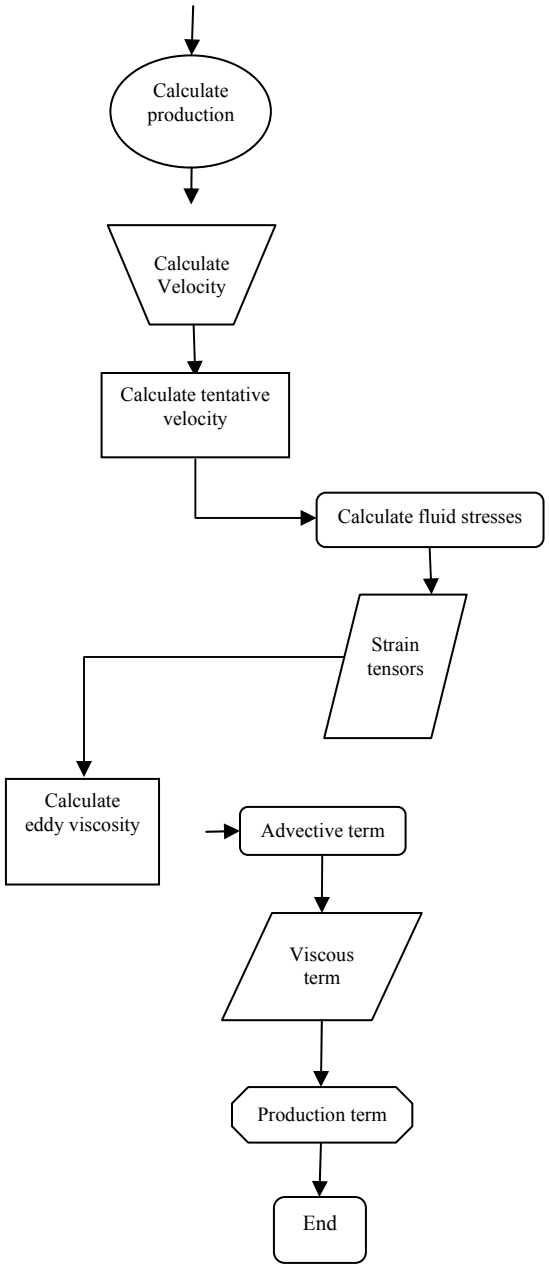
Calculate production
Calculate Velocity
Calculate tentative velocity
Calculate fluid stresses
Strain tensors
Calculate eddy viscosity
Advective term
Viscous term
Production term
End

LIST OF REFERENCES

Altinakar, M.S. (1988), Weakly depositing turbidity currents on small slopes, Ph.D. Thesis, École Polytechnique Fédérale de Lausanne, Switzerland.

Bagnold, R.A. (1962), Auto- suspension of transported sediment: Turbidity currents, Proceedings of the Royal Society of London, Series A, Mathematical and Physical Sciences, 265(1322), A discussion on progress and need of Marine Science, 315-319.

Benjamin, T.B. (1968), Gravity currents and related phenomenon, Journal of Fluid Mechanics, 31, 209-243.

Britter, R.E. and J.E. Simpson (1978), Experiments on the dynamics of the gravity current head, Journal of Fluid Mechanics, 88, 223-240.

Chu, F.H., W.D. Pilkey, and O.H. Pilkey (1979), An analytical study of turbidity current steady flow, Marine Geology, 33, 205-220.

Daly, R.A (1936), Origin of submarine "canyons", American Journal of Science, Series 5, XXXI, 186, 401-420.

Drew, D.A. (1976), Production and dissipation of energy in a turbulent flow of a particle-fluid mixture, with some results on drag reduction, Journal of Applied Mechanics, 43, 543-547.

Eidsvik, K.J. and B. Brøs (1989), Self-accelerated turbidity current prediction based upon (κ-ε) turbulence, Continental Shelf Research, 9(7), 617-627.

Elghobashi, S.E. and T.W. Abou-Arab (1983), A two-equation turbulence model for two-phase flows, Physics of Fluid, 26, 931-938.

Fine, I.V., A.B.Rabinovich, B.D Bornhold, R.E Thomson, E.A. Kulikov (2005), The Grand Banks landslide-generated tsunami of November 18, 1929: preliminary analysis and numerical modeling, Marine Geology, 215, 45-57.

Francis, J.R.D. (1957), London Engineer, 519.

Fukushima, Y., G. Parker and H.M. Pantin (1985), Prediction of ignitive turbidity currents in Scripps submarine canyon, Marine Geology, 67, 55-81.

Greimann, B.P, M. Muste and F.M. Holly (1999), Two phase formulation of suspended sediment transport, Journal of Hydraulic Research, 37(4), 479-500.

Heezen, B.C. and M. Ewing (1952), Turbidity currents and submarine slumps and the 1929 Grand Banks earthquake, American Journal of Science, 250, 849-873.

Heezen, B.C., D.B. Ericson and M. Ewing (1954), Further evidence for turbidity current following the 1929 Grand Banks earthquake, Deep Sea Research. Part I, Oceanographic research papers, 193-202.

Hsu, T.-J. (2002), A two-phase flow approach for sediment transport, Ph.D. Thesis, Cornell University, Ithaca.

Hsu, T.-J., J.T. Jenkins and P.L.-F. Liu (2003), On two-phase sediment transport: dilute flow, Journal of Geophysical Research, 108, 3057

Hsu, T.-J., J.T. Jenkins and P.L.-F. Liu (2004), On two-phase sediment transport: sheet flow of massive particles, Proceedings of Royal Society of London, A, 2223-2250.

Jenkins, J.T. and D.M. Hanes (1998), Collisional sheet flow of sediment driven by a turbulent fluid, Journal of Fluid Mechanics, 370, 29-52.

Julien, P.Y., 1995. Erosion and sedimentation, Cambridge University Press, New York.

Knapp, R.T. (1938), Energy balance in stream-flows carrying suspended load, Transactions, American Geophysical Union, 19, 501-505.

Kuenen, P.H. (1937), Experiments in connection with Daly's hypothesis on the formation of submarine canyons, Leids geologische Mededel, 8, 327-351

Lin, P.C.-P. and A.J. Mehta (1997), A study of fine sedimentation in an elongated laboratory basin, Journal of Coastal Research, SI(25), 19-30.

McTigue, D.F. (1981), Mixture theory for suspended sediment transport, Journal of the Hydraulics Division, American Society of Civil Engineers, 107, 659-673.

Middleton, G.V. (1966a), Experiments on density and turbidity currents, Canadian Journal of Earth Sciences, 3, 523-546.

Middleton, G.V (1966b), Small scale models of turbidity currents and the criterion for auto-suspension, Journal of Sedimentary Petrology, 36(1), 202-208.

Nott, P.R. and J.F. Brady (1994), Pressure-driven flow of suspension: simulation and theory, Journal of Fluid Mechanics, 275, 157-199.

Pantin, H.M. (1979), Interaction between velocity and effective density in turbidity flow: Phase-plane analysis, with criteria for auto suspension, Marine Geology, 3159-99.

Parker, G. (1982), Conditions for ignition of catastrophically erosive turbidity currents, Marine Geology, 46, 307-327.

Parker, G., Y. Fukushima and H.M. Pantin (1986), Self-accelerating turbidity currents, Journal of fluid Mechanics, 171, 145-181.

Parker, G., M. Garcia, Y. Fukushima and W. Yu (1987), Experiments on turbidity currents over an erodible bed, Journal of Hydraulic Research, 25(1), 123-147.

Plapp, J.E and J.P Mitchell (1960), A hydrodynamic theory of turbidity currents, Journal of Geophysical Research, 6, 983-992.

Schmidt, W. (1911), Zur Mechanik der Boen, Meteorologische Zeitschrift, 28, 355-362.

Simpson, J.E. (1972), Effects of the lower boundary on the head of a gravity current, Journal of Fluid Mechanics, 53, 759-768.

Simpson, J.E. and R.E. Britter (1979), Experiments on the dynamics of the front of the gravity current, Proceedings of the 2nd International Symposium on Stratified Flows, The Norwegian Institute of Technology, Trondheim, 174-183.

Simpson, J.E. and R.E. Britter (1980), A laboratory model of an atmospheric mesofront, Quarterly Journal of Royal Meteorological Society, 106, 485-500.

Simpson, J.E. (1987), Gravity currents: In the environment and the laboratory, Ellis Horwood, England.

Richardson, J.F. and W.N. Zaki (1954), Sedimentation and fluidization. Part 1, Transation of the Institution of Chemical Engineers, 32, 35-53.

Rodi, W. (1984), Turbulence models and their application in hydraulics: A state of the art review, International Association of Hydraulic Engineering and Research. Delft.

Von Karman, T. (1940), The engineer grapples with non-linear problems, Bulletin of the American Mathematical Society, 46, 615-683.

Winterwerp, H. (1999), On the dynamics of high-concentrated mud suspensions, Communications on Hydraulic and Geotechnical Engineering, Delft University of Technology, The Netherlands.

BIOGRAPHICAL SKETCH

Gowtham Krishna was born in 1982, Mysore, India. He completed his undergraduate education in 2006 from the Jawaharlal Nehru Technological University, Hyderabad, in Mechanical Engineering in 2006. After briefly working in the industry, he joined the University of Florida in the Spring term of 2007.